TION PAGE

Form Approved
OMB No. 0704-0188

1. AGENCY USE ONLY (Leave blank)	2. REPORT DATE	3. REPORT TYPE AND DATES COVERED
	3-30-94	Final 6/1/90 - 12/31/93

4. TITLE AND SUBTITLE
Analog Processing of Optical Wavefronts Using Integrated Guided-Wave Optics

5. FUNDING NUMBERS
F49620-90-C-0036
3151/00

6. AUTHOR(S)
Dr. Robert H. Rediker

7. PERFORMING ORGANIZATION NAME(S) AND ADDRESS(ES)
Research Laboratory of Electronics
Massachusetts Institute of Technology
77 Massachusetts Avenue
Cambridge, MA 02139

8. PERFORMING ORGANIZATION REPORT NUMBER
AFOSR-TR- 94 0306

9. SPONSORING/MONITORING AGENCY NAME(S) AND ADDRESS(ES)
Air Force Office of Scientific Research
Building 410
Bolling Air Force Base, DC 20332

10. SPONSORING/MONITORING AGENCY REPORT NUMBER
3151/00

11. SUPPLEMENTARY NOTES
The view, opinions and/or findings contained in this report are those of the author(s) and should not be construed as an official Department of the Army position, policy, or decision, unless so designated by other documentation.

12a. DISTRIBUTION/AVAILABILITY STATEMENT
Approved for public release; distribution unlimited.

12b. DISTRIBUTION CODE

13. ABSTRACT *(Maximum 200 words)*

Work by Dr. Rediker and his collaborators is summarized here

14. SUBJECT TERMS	15. NUMBER OF PAGES
	16. PRICE CODE

17. SECURITY CLASSIFICATION OF REPORT	18. SECURITY CLASSIFICATION OF THIS PAGE	19. SECURITY CLASSIFICATION OF ABSTRACT	20. LIMITATION OF ABSTRACT
UNCLASSIFIED	UNCLASSIFIED	UNCLASSIFIED	UL

RESEARCH LABORATORY OF ELECTRONICS
MASSACHUSETTS INSTITUTE OF TECHNOLOGY
CAMBRIDGE, MASSACHUSETTS 02139

Analog Processing of Optical Wavefronts Using Integrated Guided-Wave Optics

Contract #F49620-90-C-0036

Final Report
Period Covered June 1, 1990 -- December 31, 1993

Submitted to the U.S. Air Force - Office of Scientific Research

Dr. Robert H. Rediker, Principal Investigator

March 31, 1994

Table of Contents

ANALOG PROCESSING OF OPTICAL WAVEFRONTS USING INTEGRATED GUIDED-WAVE OPTICS

Final Report to the Air Force Office of Scientific Research
Contract #F49620-90-C-0036

June 1, 1990 -- December 31, 1993

Robert H. Rediker

Massachusetts Institute of Technology
Department of Electrical Engineering and Computer Science
and Research Laboratory of Electronics

I. Introduction

Integrated Guided-Wave Optics has many advantages for the analog processing of optical wavefronts. These include small-size, high-speed, simplicity, reliability and reproducibility. The fabrication technique is similar to that of integrated circuits. The thrust of this program was to develop an integrated guided-wave optic system in GaAs and GaAlAs for use at GaAs laser wavelength, to remove aberrations from a laser beam and to steer the beam The system would in addition have the capability to appropriately phase the outputs from a multiplicity of power amplifiers or injection locked lasers. It was also the intent of the program to design and build the optical circuits so they are compatible with on-chip electronic circuits in order to minimize the required number of off-chip leads.

The research program was proposed by MIT Research Laboratory of Electronics with part of the work being performed at MIT Lincoln Laboratory. In general, guided-wave component evaluation, analysis and understanding of optimization was performed at MIT Research Laboratory of Electronics, while fabrication and actual optimization was performed at MIT Lincoln Laboratory.

It has been shown that integrated guided-wave optics can successfully be employed to measure and/or modify optical wavefronts.[1] The electrooptic material used was Ti:$LiNbO_3$. Recently, however, there have been significant advances in the use of semiconductor as the electrooptic material which integrated optical devices are fabricated.[2] This program explored the fundamental issues associated with optical wavefront correction using integrated guided-wave devices in GaAlAs for use at GaAs/GaAlAs laser wavelengths.

In Section IIA the concept for correction of an optical wavefront is presented and several obvious advantages of "on-chip processing" are pointed out. Section IIB describes the operation of the basic integrated-optics module for integrated guided-wave optics systems to do the required wavefront correction and steering.

The success of this program and many other integrated optics programs depends on the efficient collection of incident light and the efficient emission of laser light from the semiconductor. The fabrication, operation and optimization of reduced-confinement GaAlAs tapered waveguide antenna for use in coupling to free-space radiation was described[3,4], and described in detail in our final report for the predecessor Air Force Contract #F49620-87-C-0043.

In this Contract we addressed two major tasks. In the first we focused our attention on the requirements for optical phase difference measurement and correction at the wavelength of operation specific to the thrust of our program. In the second major task we addressed the fabrication of the basic integrated-optics module for integrated guided-wave optics systems to do the required wavefront correction and steering.

Sections III and IV address the first task. Section III describes the theory behind the design and development of an optical phase difference measurement technique that is independent of the power or power ration in the interferometer arms. This technique has been incorporated into a proof-of-concept Mach Zehnder interferometer to demonstrate

phase measurement and correction in a feedback system. In Section IV experimental results obtained with the proof-of-concept Mach Zehnder interferometer are presented.

The second task is described in Sections V and VI. The fabrication and the evaluation of the basic integrated-optics module are addressed. The fabrication techniques were optimized so all the various required electrooptic components could be built on the same substrate. In addition, the techniques were developed so the photodiode to measure the interferometer output was also fabricated on the same on the same substrate. Great care was taken in the design and fabrication of the basic integrated-optics module so that in a further step (not taken at this time) integrated circuitry could be added on the same semiconductor chip to perform all the circuit functions required.

II. The Basic Module

A. Concept

The basic module proposed for wavefront correction is shown in Fig. 1. The system could contain as few as ten modules or as many modules as limited by reliability and reproducibility or other system considerations. Figure 1 is the same as Fig. 6 in the U.S. patent[5] issued to the principal investigator, except is also includes the on-chip detector, voltage comparator and feedback control system. The advantages of this "on-chip processing" are the reduction of the number of leads that are required to come off the chip and the reduction of complexity of off-chip processing and time delays in signal transmission and processing. For example, in a system with 10^3 modules, only one control set-voltage is required (one lead). Without on-chip processing 10^3 voltages V_N need to be determined by the off-chip processor and require up to 10^3 leads to impress these voltages. It should be pointed out that there is a 2π radians (360°) ambiguity in the phase of the output from any waveguide. The voltage, V_N, need never exceed $V_{2\pi}$, the voltage across the waveguide electrodes to produce a change in the phase of 2π radians. Of course the incoming aberrated beam will be distorted by much

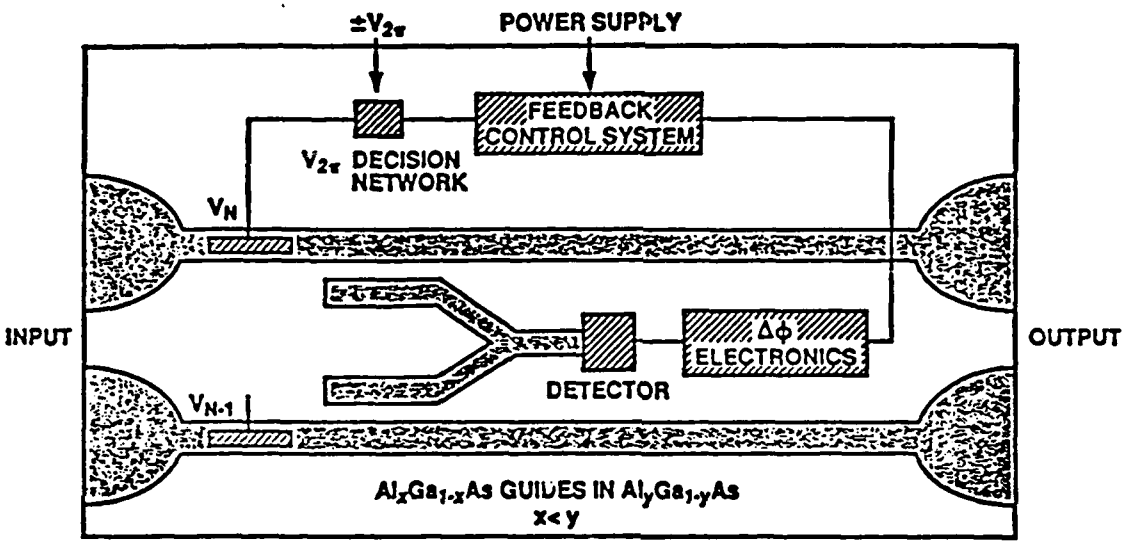

Fig. 1 The basic module for wavefront correction. In practice of the order of 10^3 modules may be appropriate for high-resolution correction. A significant advantage of the concept is the on-chip processing which reduces dramatically the number of leads required to come off the chip. The guides have a lower fraction, x, of Al in the $Al_xGa_{1-x}As$ than the fraction, y, in the substrate for dielectric confinement of the electromagnetic wave.

more than 2π radians over the aperture 10^3 modules. A second lead to the chip is required for on-chip $V_{2\pi}$ correction to keep all V_N to correspond to phase shifts between 0 and 2π. For example if the aberration over the aperture is 50π and $V_{2\pi} = 20$ V, then without the successive $V_{2\pi}$ correction V_N would equal 500 V, which is not feasible for many fundamental and practical reasons.

While the module shown in Fig. 1 is specific to removing aberrations in the wavefront or steering the beam, using the same basic components other figures in the aforementioned patent illustrate the focusing of the wavefront. In general, analog processing of the optical wavefront is possible with various configurations of the components illustrated in Fig. 1.

B. The Operation of the Basic Module

The operation of the basic module in Fig. 1 is as follows: The voltage V_N delays the phase of the optical wave in waveguide N by ϕ_N and the voltage V_{N-1} delays the phase of the optical wave in waveguide (N-1) by ϕ_{N-1} so that the two waves emerge from the waveguides in phase (the aberration is removed) or at a predetermined phase (the aberration is removed and the beam is steered). Evanescent wave coupling is used to couple a small fraction δ of the power in each straight-through waveguide to the adjacent arm of the interferometer between the waveguides. For equal incident optical powers, $\mathcal{P}$, incident on each waveguide and equal evanescent coupling, δ, to each interferometer arm, the optical power incident on the detector is

$$P_{\Delta\phi} = [2\delta\mathcal{P} \cos^2 \frac{\phi_N - \phi_{N-1}}{2}] B \qquad (1)$$

where B takes into account additional losses in interferometer arms such as due to the bends. When the powers $\mathcal{P}$ are unequal and/or the couplings δ, are unequal eq. (1)

contains additional terms as is discussed in Section III below. Also presented in Section III are techniques to measure ($\Delta\phi = \phi_N - \phi_{N-1}$) independent of the powers $\mathcal{P}$, the couplings δ and the losses taken into account by B. In integrated optics as in integrated circuits it is important for operation to be independent of individual component variations. For maximum output of the detector in Fig. 1 the feedback control system will set the value of V_N with respect to $V_{(N-1)}$ so that the phase shift ($\phi_N - \phi_{N-1}$) between the outputs of the two straight waveguides is zero. The details of the feedback control system are not described here, except to mention that it is a relatively straightforward system which nulls the detector output. As part of the electronic circuit, as mentioned earlier, there is a "$V_{2\pi}$ decision network" to reduce V_N below the maximum voltage $V_{2\pi}$ which produces a phase shift of 2π radians (360 °). Subtracting (or adding if V_N is negative) $V_{2\pi}$ does not change the phase of the output from the straight-through waveguide.

III. Theory of Wavefront Phase Tilt Measurement

In the wavefront sensing and correction basic module, the input powers to the interferometer arms will not be equal as a result of input power nonuniformity or unequal coupling by the evanescent couplers. The requirement that the coupling of the evanescent couplers be equal for a system with a large number of modules (10^3 - 10^4) is unrealistic. In integrated optics, as in integrated circuits, it is important to relax the requirements on individual components and require that the operation of the integrated optics (circuits) be independent of significant component variations. Therefore an optical wavefront phase tilt measurement technique has been developed to measure the wavefront phase tilt regardless of power non-uniformity.

The output of a Y-junction interferometer with equal powers in the input arms is given by Equation 1. For unequal powers and unequal evanescent coupling from the

straight-through waveguides to the interferometer arms, the output power of the Y-junction is given by,

$$P_{out} = [\delta_1 P_1 + \delta_2 P_2 + 2\sqrt{\delta_1 P_1 \delta_2 P_2}\cos\phi]\, B \qquad (2)$$

where $\mathcal{P}_1$ and $\mathcal{P}_2$ are the unequal incident powers, δ_1 and δ_2 are the unequal coupling coefficients of the evanescent power couplers, B again accounts for additional losses in the interferometer arms, and ϕ is the phase difference between the arms. Extracting the phase difference ϕ from this equation required measuring the powers in the output arms, the coupling from each evanescent coupler, and the loss in the arms of the interferometer.

The Y-junction interferometer technique, shown in Fig. 2, used for the phase measurement is similar to dither techniques used in optical fiber sensors[6] and phase-locked interferometry.[7] If a sinusoidal phase dither $\Gamma \sin \omega t$ is applied to one arm of a Y-junction interferometer, the detected output power $\mathcal{P}_{\Delta\phi}$ is given by

$$P_{\Delta\phi} = (P_1 + P_2)/2 + \sqrt{P_1 P_2}\cos(\Delta\phi - \Gamma \sin \omega t) \qquad (3)$$

where $\mathcal{P}_1$ and $\mathcal{P}_2$ are the powers in the interferometer arms and $\Delta\phi$ is the phase difference between the arms. By using a Bessel function expansion for the cosine-sine term in Eq. (3), the following expressions for the amplitudes of the first $A(\omega)$ and second $A(2\omega)$ harmonics are obtained:

$$A(\omega) = 2\sqrt{P_1 P_2}J_1(\Gamma) \sin \Delta\phi \qquad (4a)$$

$$A(2\omega) = 2\sqrt{P_1 P_2}J_2(\Gamma) \cos \Delta\phi \qquad (4b)$$

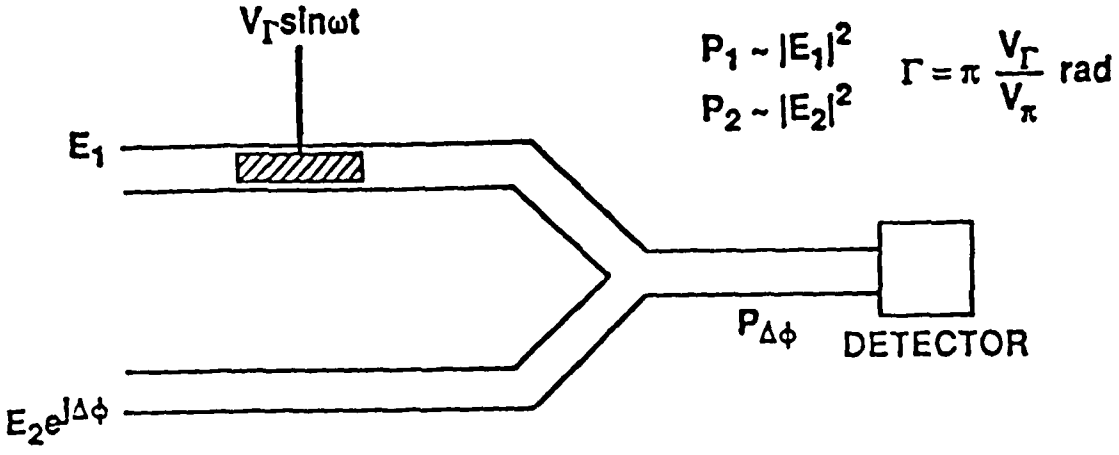

Fig. 2 Y-junction optical phase difference measurement technique that is independent of the input power or power ratio of the interferometer arms.

where $\mathcal{J}_1(\Gamma)$ and $\mathcal{J}_2(\Gamma)$ are Bessel functions of the first kind of order 1 and 2 respectively. The phase difference between the arms can then be calculated using

$$\Delta\phi = \arctan\left[\frac{A(\omega)}{A(2\omega)}\frac{J_2(\Gamma)}{J_1(\Gamma)}\right] = \arctan\left[\frac{A(\omega)}{A(2\omega)}\frac{\frac{\Gamma^2}{8} - \frac{\Gamma^4}{96} + \cdots}{\frac{\Gamma}{2} - \frac{\Gamma^3}{16} + \cdots}\right] \quad (5)$$

where the number of significant terms required to evaluate the Bessel functions depends on the amplitude of the phase dither Γ. Note that the calculated phase difference is independent of the power or power ration in the input arms of the interferometer.

This technique was incorporated into a proof-of-concept AlGaAs Mach-Zehnder interferometer, shown Fig. 3, to demonstrate phase measurement and correction. The input power is divided between the interferometer arms. Phase modulators are used to apply a sinusoidal phase dither, to set a phase difference between the arms, and to correct the phase difference. A high voltage V_{abs} applied to the fourth modulator creates a power imbalance by absorbing power in one arm via electroabsorption, in addition to a phase change. $P_{\Delta\phi}$ is detected off chip, the amplitudes of the first and second harmonics are measured, $\Delta\phi$ is calculated for the ratio, and $V_{correct}$ is updated. The dc output if the interferometer, which is a maximum when $\Delta\phi$=0, is also monitored. While the final goal is to monolithically integrate the optical and electronic components, this system utilizes off-chip circuitry and computer control of the feedback loop.

The interferometer was fabricated using a dielectric-loaded strip waveguide structure, illustrated in Fig. 4. The epilayers were grown by organometallic vapor phase epitaxy and the rib was etched in the upper cladding of the waveguide structure by

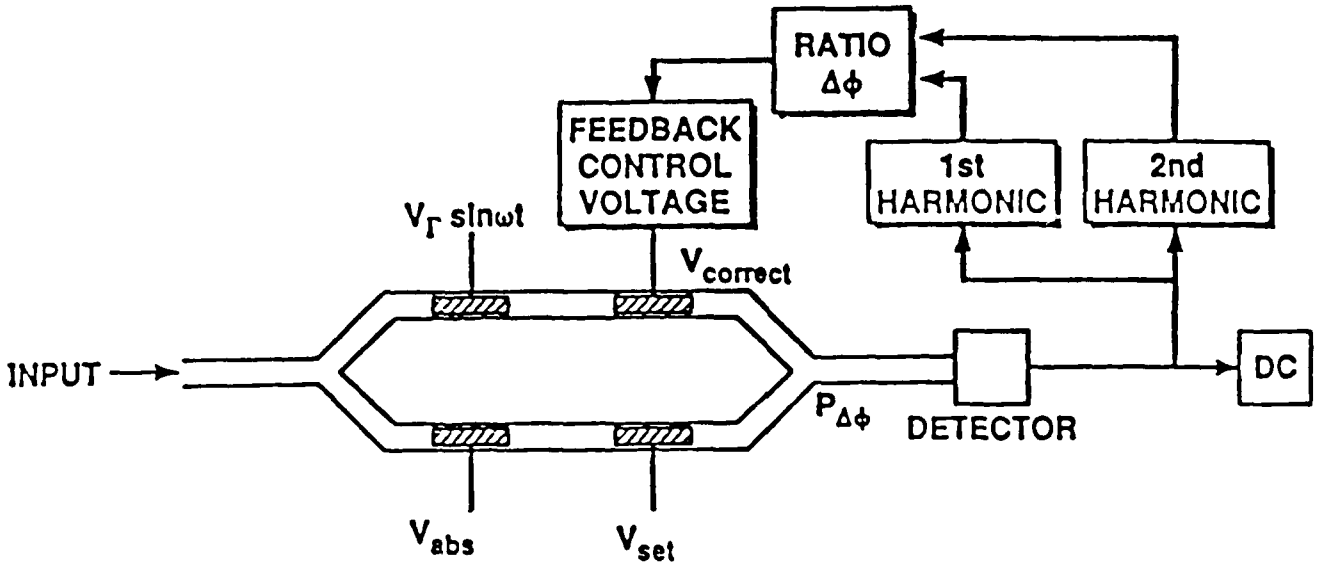

Fig. 3 Proof-as-concept AlGaAs Mach-Zehnder interferometer system for demonstrating phase measurement and correction independent of power or power ratio in the interferometer arms.

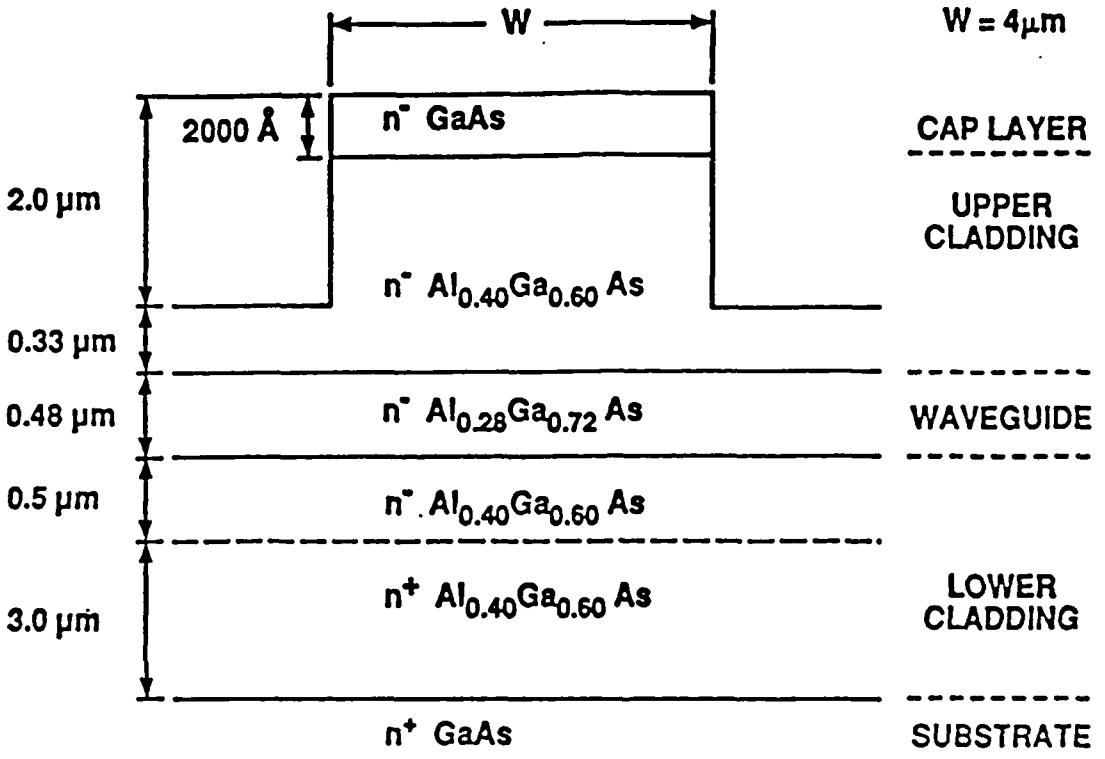

Fig. 4 Cross section of the dielectric-loaded strip hetrostructure waveguide for use at GaAs wavelengths. For the phase modulator sections, part of the upper cladding was doped p^+ (with the p^+-n junction located about 0.5 μm from the waveguide-cladding interface), and a AuZnAu top contact was used.

chlorine reactive ion etching for two-dimensional optical confinement. This four-layer structure was modeled theoretically and single-mode waveguides designed to minimize absorption loss (low carrier concentration in the waveguides layer), scattering loss (the optical mode is away from the etched interfaces), and radiation loss in abrupt bends and Y-junctions (the optical mode is well confined). The waveguide propagation loss was <1 dB/cm measured at 862 nm by a Fabry-Perot technique.[8] Measurements were made to characterize the angular dependence of the abrupt bend insertion loss and Y-junction insertion loss and are shown in fig. 5. For the maximum angles used in the Mach-Zehnder interferometers, the abrupt bend insertion loss was ~ 0.20 dB/bend for a 0.5 degree angle and the Y-junction insertion loss was 0.37 dB for a 1.0 degree full angle.

Phase modulators were fabricated by a selective Be ion implantation, followed by rapid thermal annealing, to form a p^+-n-n^+ structure. The phase in the waveguides was modulated via the electrooptic effect by reverse biasing the p-n structure. The V_π voltage of these phase modulators was ~ 6.8 V for a 2 mm modulator. The composition of the epilayers was chosen to minimize electroabsorption at the desired operating wavelengths and voltages. These phase modulators were modeled both by a perturbation analysis and a more exact analysis of the waveguides in the presence of an electric field. Measurements by photoluminescence (to determine composition), stripping Hall (to determine p-n junction depth), and C(V) [to determine carrier concentration profile] were used to model fabricated devices. A comparison of the theoretical analyses for phase modulation and experimental results for a 2 mm modulator are shown in Fig. 6.

The breakdown voltage of these phase modulators was ~ 47 V, so a maximum applied voltage of 42 V was chosen for these experiments. The correction voltage was limited to a range slightly larger than $V_\pi/2$ to $5V_\pi/2$, corresponding to a range in phase shift slightly larger than 2π. This was done to ensure that the modulator was always reverse biased and to minimize electroabsorption. The sinusoidal phase dither was applied to a 1 mm modulator (with V_π ~ 12.4 V). Typically, the dither signal had a peak

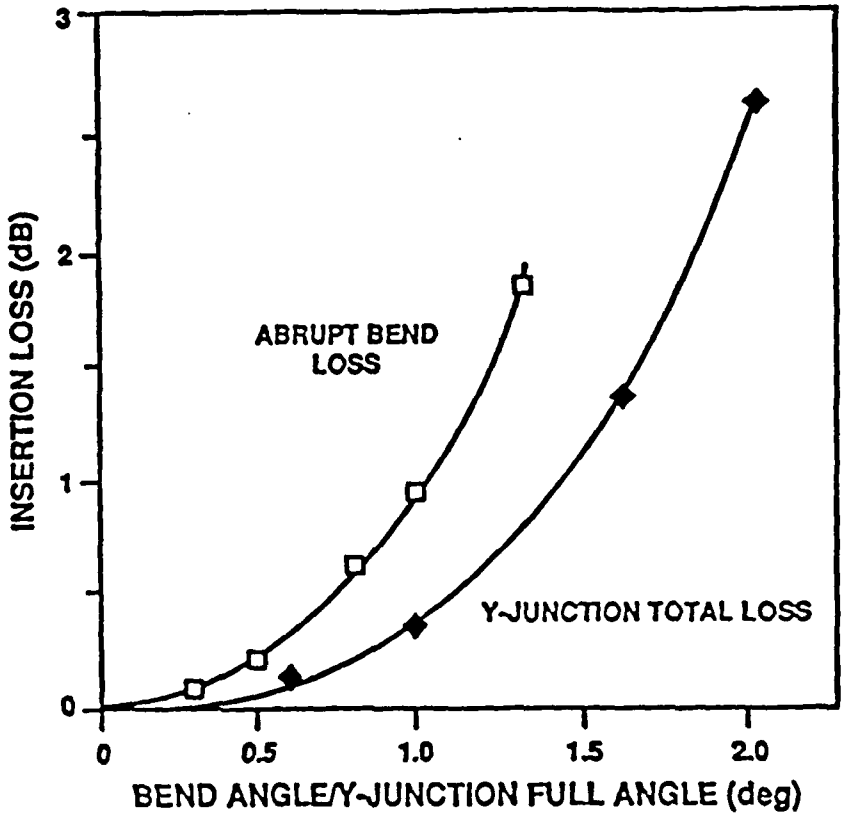

Fig. 5 Measurements of the angular dependence of the abrupt bend insertion loss and Y-junction insertion loss.

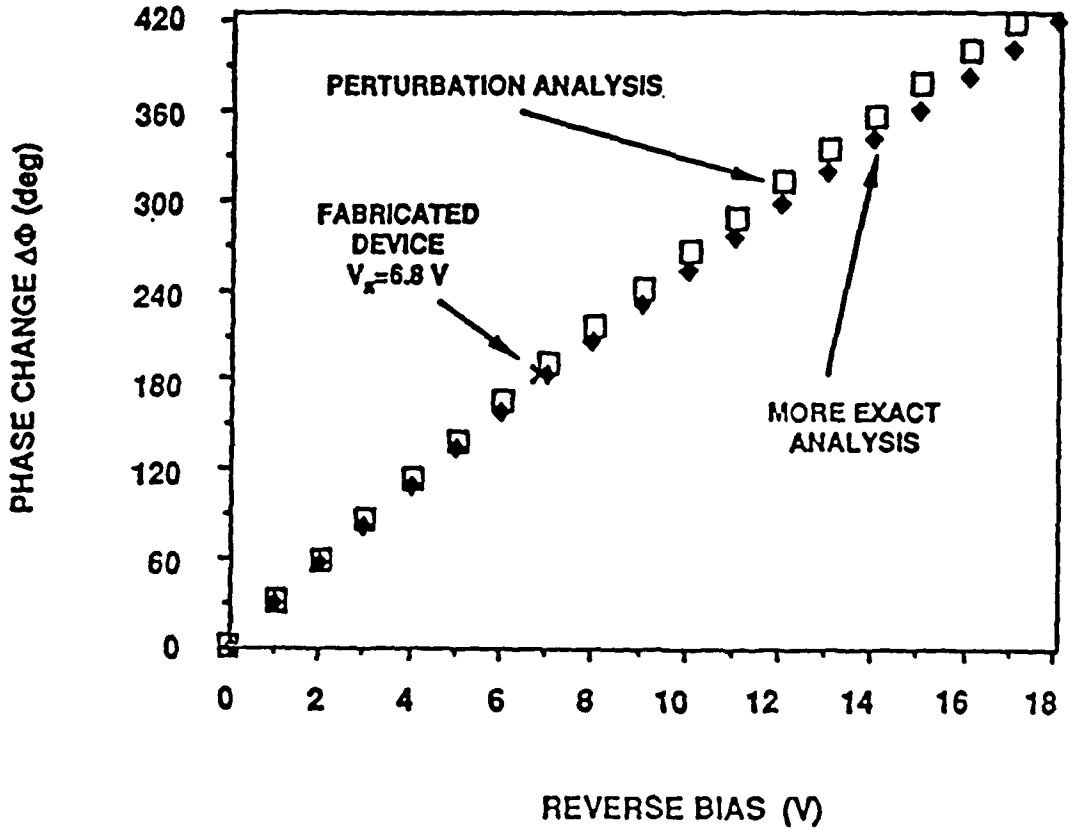

Fig. 6 Comparison of the experimental results measured for a 2 mm long modulator with the modulation predicted by the perturbation and more exact analyses.

voltage amplitude V_Γ of 1.0 V (amplitudes of up to 5.0 V have been used) and a frequency of 500 Hz. The Bessel functions in Eq. (5) were calculated using the first two terms and the simple linear relationship for the amplitude of the phase dither $\Gamma = \pi V_\Gamma / V_\pi$. The experimental set-up used for testing the Mach-Zehnder interferometers is shown in Fig. 7. The output can be directed using the switching mirror of a microscope to either a CCD camera for observation, or to a detector for power output measurements. Probe stations were usually used to apply voltages to the four phase modulators.

IV. Experimental Demonstration of Phase Difference Measurement and Correction

A. Modes of Operation

The Y-junction Mach-Zehnder interferometer system was operated in two modes: a no-feedback mode and a feedback mode. The no-feedback mode of operation characterized the measurement of an applied phase difference between the arms of the interferometer, while the feedback mode demonstrated the measurement and correction of an applied phase difference between the interferometer arms. The data plotted in this section for the dc and the amplitudes of the first and second harmonics, was normalized by the appropriated maximum shared value, for convenience.

1. No Feedback Mode

The interferometer system was initially operated without feedback, shown in Fig. 8, to characterize the phase measurement technique as a function of voltage-induced phase differences. A voltage V_{set} was applied to one arm to create a phase difference between the interferometer arms, and the amplitudes of the first and second harmonics were measured and used to calculate $\Delta\phi$. The interferometer dc output was also monitored. The voltage V_{set} was successively stepped from zero to 42 V in steps of .25 V, and the measurements repeated for each step (shown in Fig. 9). As V_{set} was increased above 25 V, a decrease in the peak amplitude of the dc output and the second harmonic indicated that the power in the V_{set} arm decreased because of

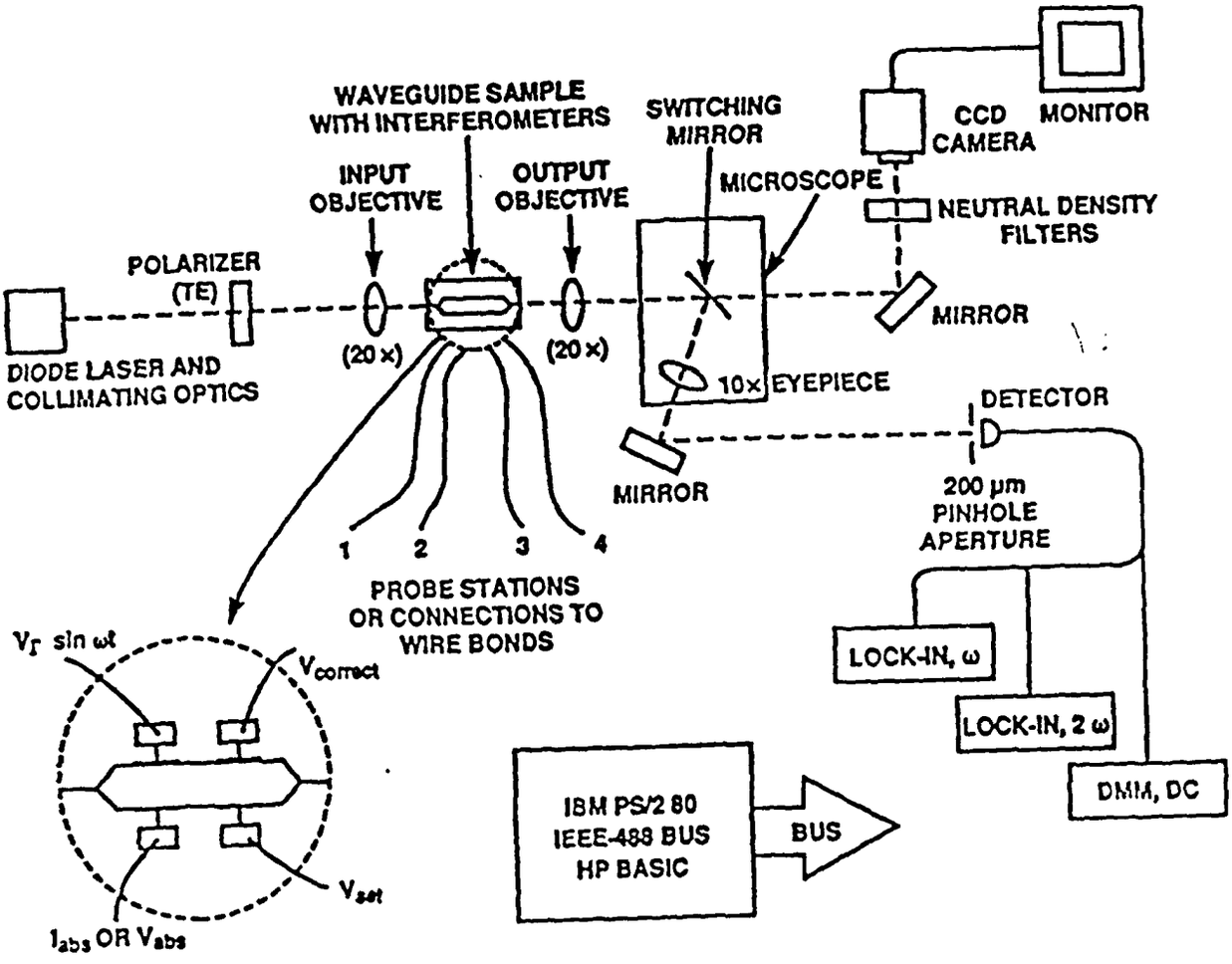

Fig. 7 Experimental set-up for demonstrating optical phase difference measurement and correction using a proof-of-concept Mach-Zehnder interferometer.

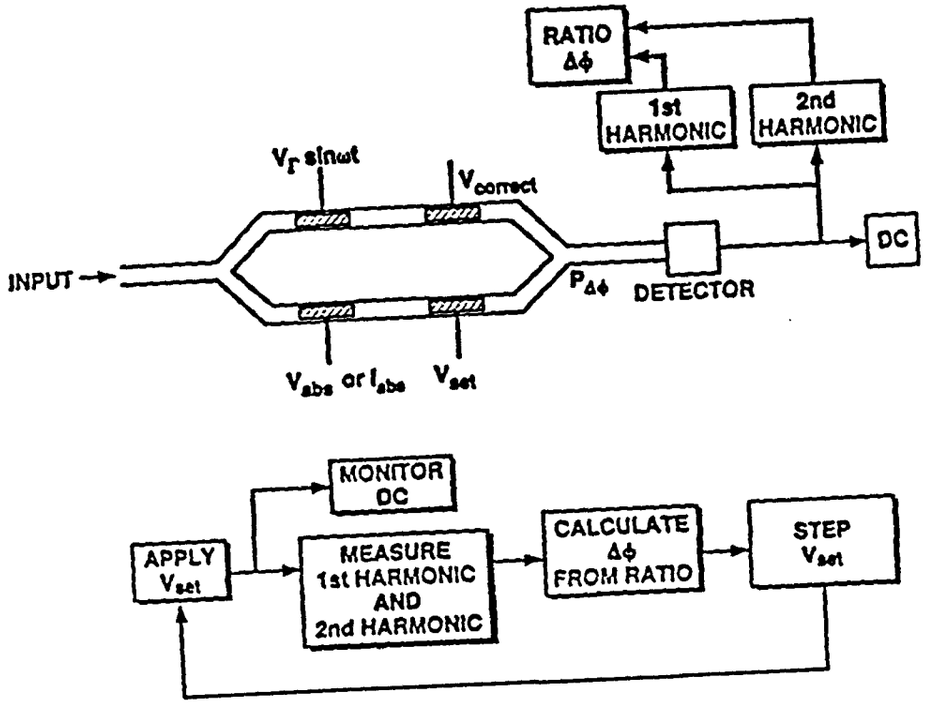

Fig. 8 No-feedback mode of operation to characterize the phase measurement technique.

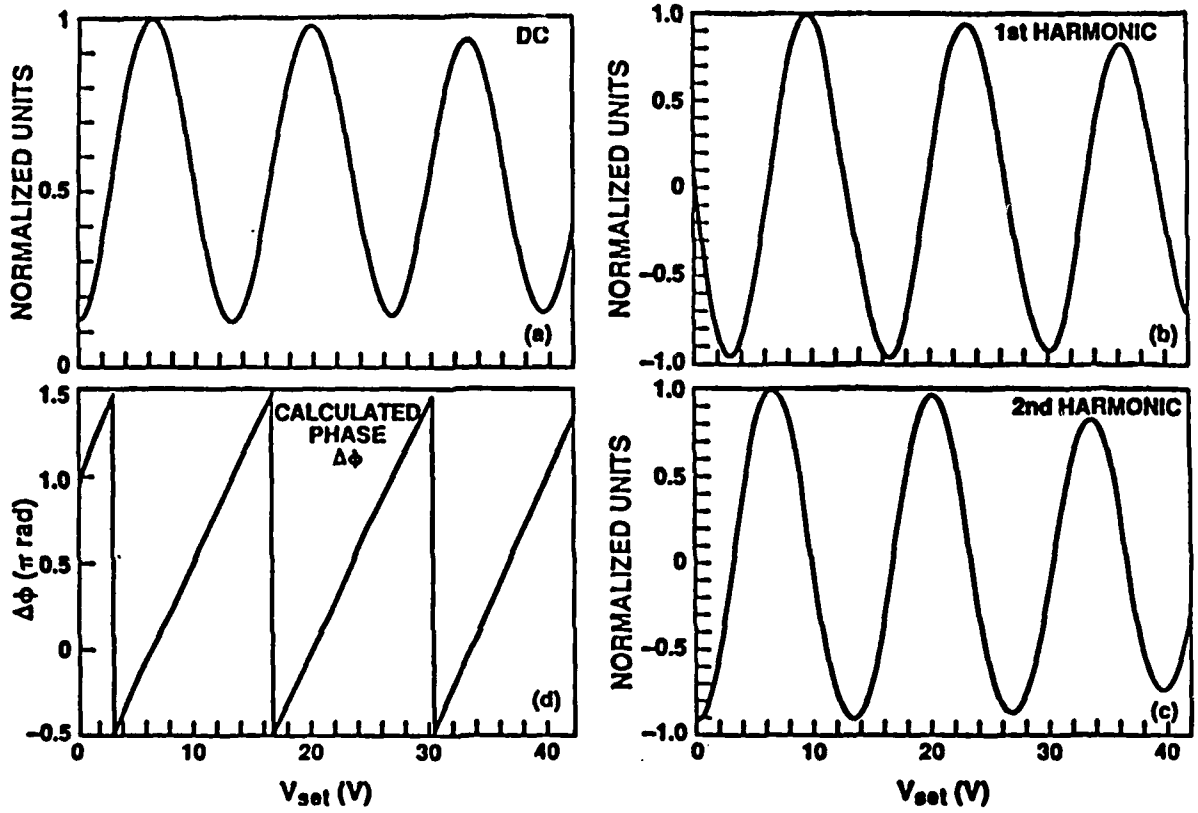

Fig. 9 Results for the Mach-Zehnder interferometer in the no-feed-back mode: (a) the measured dc amplitude, (b) the measured amplitude of the first harmonic, (c) the measured amplitude of the second harmonic, and (d) the calculated phase difference Df between the interferometer arms.

electroabsor[illegible]tion. For calculation purposes, the phase difference between the interferometer arms was assumed to always be between $-\pi/2$ and $3\pi/2$. The choice of phase range was arbitrary and could be any 2π range. Arbitrarily keeping $\Delta\phi$ between $-\pi/2$ and $3\pi/2$ results in a 2π phase jump at $3\pi/2$. The calculated $\Delta\phi$ increased linearly with V_{set} over each $-\pi/2$ to $3\pi/2$ range and was in agreement with the observed cosine-squared dependence of the dc output of the Mach-Zehnder interferometer.

2. Feedback Mode

With feedback, as shown in Fig. 10, a phase difference was again created by applying V_{set}, the first and second harmonics were measured, and $\Delta\phi$ was calculated. If $\Delta\phi$ was not zero, $V_{correct}$ was updated, the harmonics were remeasured, and the new $\Delta\phi$ was calculated. This process was repeated until $\Delta\phi$ equaled zero, that is, until the phase difference between the arms had been corrected. For the results of this section, phase differences were corrected to less than 0.0044 rad (or .25 °). A new V_{set} could then be applied and the correction process repeated. The correction voltage was updated by assuming a simple linear relationship between phase and applied voltage. $\Delta\phi$ was divided by 2π and multiplied by the $V_{2\pi}$ voltage, and this result was added to the old correction voltage. The remainder of the update procedure consisted of limit checks (by adding or subtracting $V_{2\pi}$) to ensure that the correction voltage was within the specified range (from $V_\pi/2$ to $5V_\pi/2$).

Successive Steps in Phase Difference

For the case shown in Fig. 11, V_{set} was increased in successive steps from 0 to 20 V. For each value of V_{set}, the first and second harmonics were measured and the phase calculated. Each step in V_{set} resulted in a corresponding increase in the phase difference, followed by phase-correcting cycles until $\Delta\phi = 0$ and phase correction had been attained. As expected, the amplitude of the second harmonic (shown in Fig. 11(c)) and the dc output (shown in Fig. 12(b)) decreased as each V_{set} increment was applied, and were maximized when the phase difference was corrected. Figure 12(a) shows the

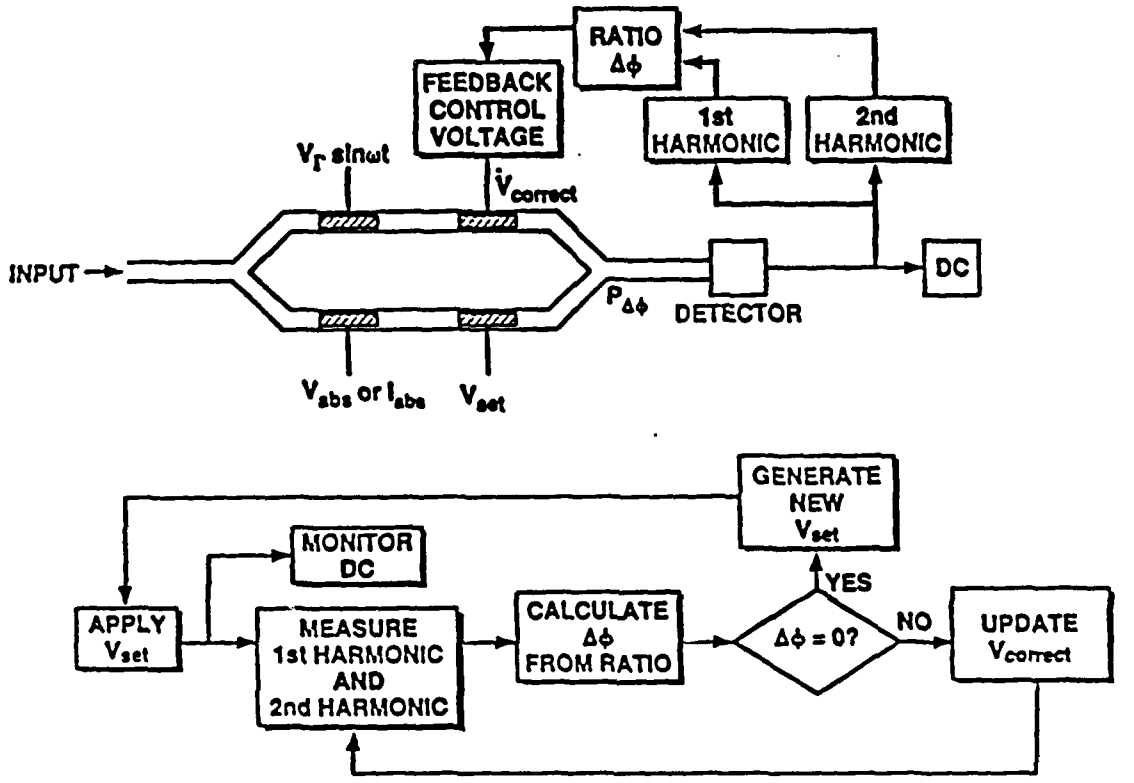

Fig. 10 Feedback mode of operation to demonstrate the measurement and correction of an applied phase difference between the arms of the interferometer.

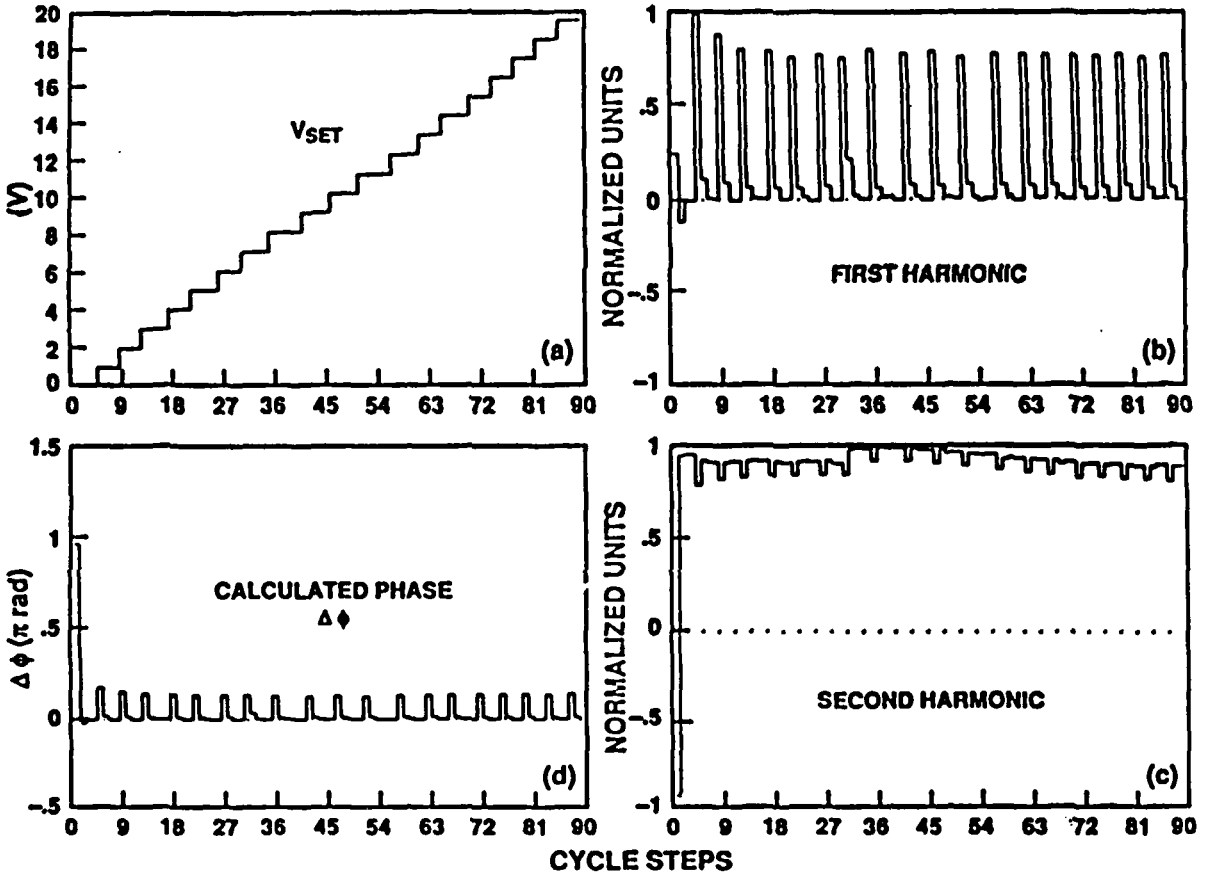

Fig. 11 Results for operation of the Mach-Zehnder interferometer system in the feedback mode: (a) V_{set} successively stepped from zero to 20 V, (b) the measured amplitude of the first harmonic, (c) the measured amplitude of the second harmonic, and (d) the calculated phase difference $\Delta\phi$ between the interferometer arms.

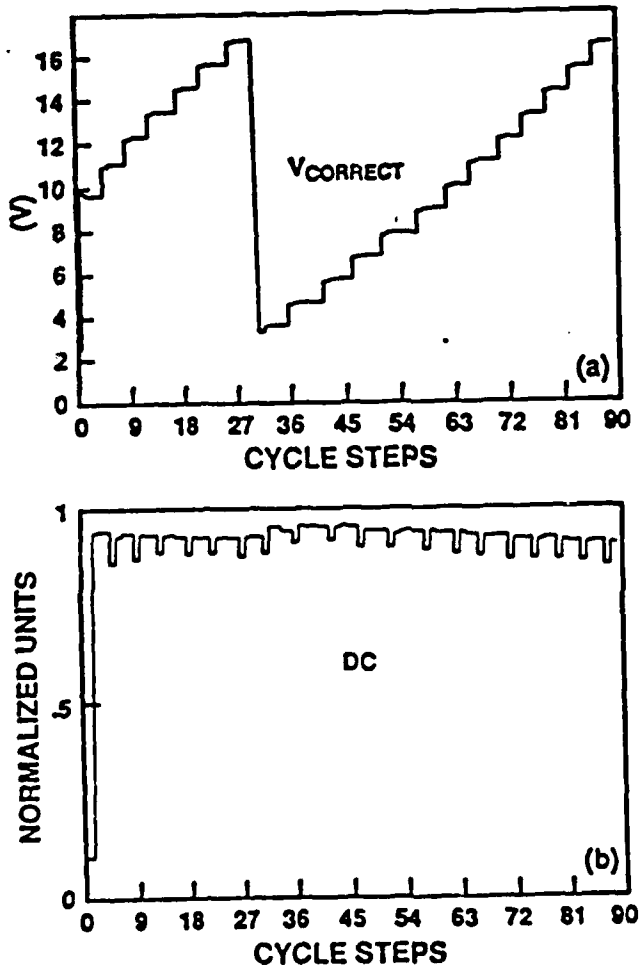

Fig. 12 Results for operation in the feedback mode with V_{set} successively stepped from zero to 20 V: (a) the applied correction voltage $V_{correct}$, and (b) the measured dc amplitude.

updated $V_{correct}$ that was applied to correct the calculated $\Delta\phi$. Note that a $V_{2\pi}$ subtraction was required to keep $V_{correct}$ in the specified range. Phase correction was achieved to within 0.0044 rad (or .25°). Correction was usually attained in 2 to 3 cycles for each step in an applied phase increment. Further improvements could be obtained with more sophisticated algorithms for the phase modulator characteristics (including any nonlinear effects). In this demonstration, the cycle time for each phase-correcting cycle was a few seconds. This can be easily reduced to the order of milliseconds by increasing the dither frequency and using faster feedback electronics.

Random Phase Differences

Results were also obtained for the case where a random number generator was used to generate random values for V_{set} (shown in Fig. 13), which resulted in random values for V_{set} (shown in Fig. 13), which resulted in random phase differences being applied between the interferometer arms. Phase correction occurred in 2 to 3 cycles.

B. Intentional Power Imbalance Between Interferometer Arms

In this section, the measurement and correction of an applied phase difference is described for cases of intentional power imbalance (with power ratios greater than 10:1) between the arms of the interferometer. A power imbalance between the interferometer arms was created either by electroabsorption and/or free carrier absorption in the V_{set} arm. These results were obtained using a Mach-Zehnder interferometer in which the lower arm (see Fig. 3) had one modulator 1 mm long and the second modulator 2 mm long.

Figure 14 shows the results for the Mach-Zehnder interferometer operated in the feedback mode where V_{set} was applied to the 2 mm modulator and successively stepped from zero to 10 V in 1.0 V steps. For this sample, phase measurements and correction were typically accomplished in 3-4 cycles. These results are similar to those in the previous section, and are presented here to serve as a comparison for the cases of phase

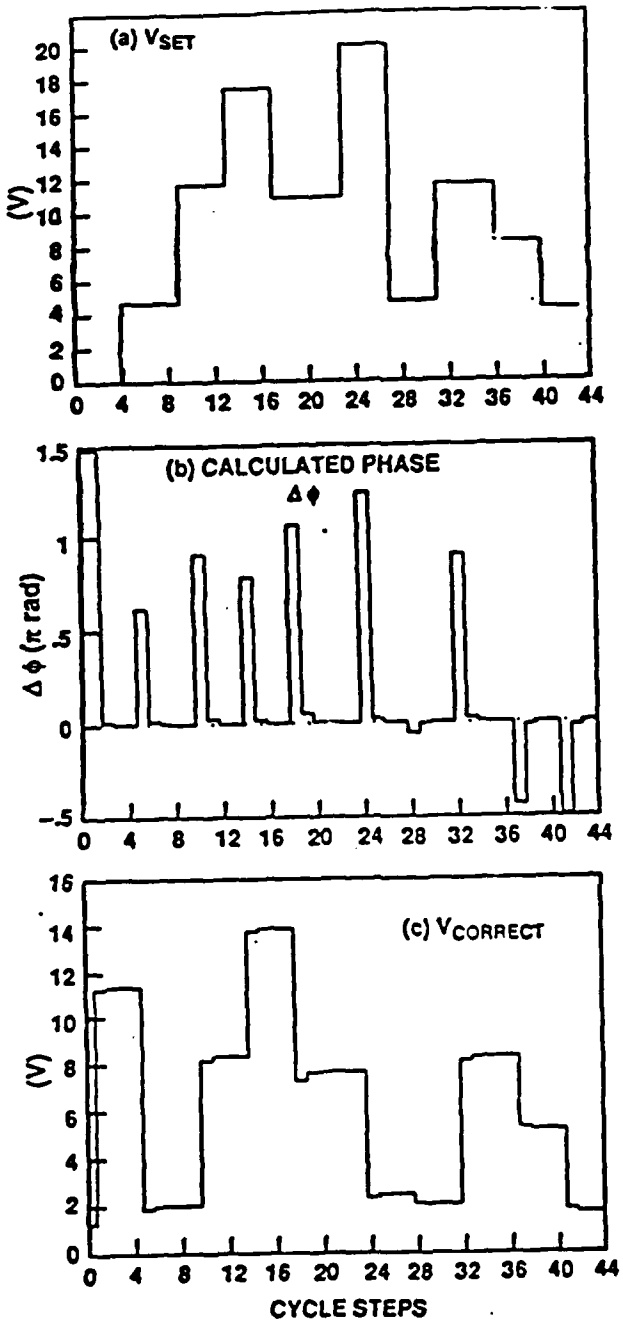

Fig. 13 Results for operation in the feedback mode: (a) V_{set} generated by a random number generator, (b) the calculated phase difference $\Delta\phi$ between the interferometer arms, and (c) the applied correction voltage $V_{correct}$.

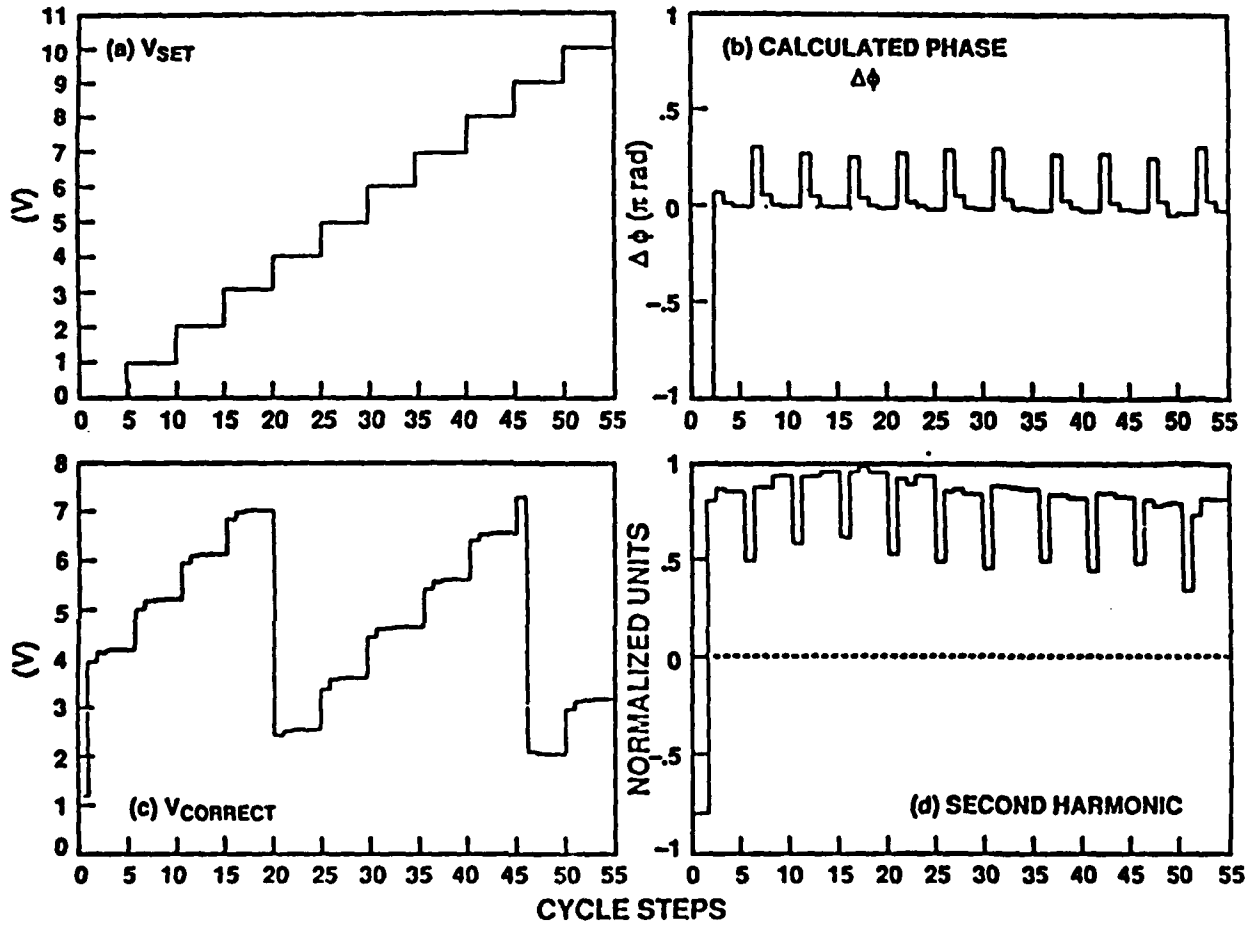

Fig. 14 Phase measurement and correction results for the 1.0 degree Y-junction Mach-Zehnder interferometer in Set 6 of sample 961-1: (a) V_{set} successively stepped from zero to 10 V, (b) the calculated phase difference $\Delta\phi$ between the interferometer arms, (c) the applied correction voltage $V_{correct}$, and (d) the measured amplitude of the second harmonic.

measurement and correction with intentional power imbalance which will be presented later in this section.

The amplitude of the second harmonic is proportional to the square root of the product of powers in the interferometer arms $(P_1 P_2)^{1/2}$ (see Eq. 4b). Thus, if power is absorbed only in the V_{set} arm of the interferometer, then the power loss in that arm can be estimated from the square of the decrease in the amplitude of the second harmonic at the of phase correction by

$$L = 1 - \left[\frac{A(2\omega)_{corr}}{A(2\omega)_{max}}\right]^2 \qquad (6)$$

where $A(2\omega)_{corr}$ is the measured amplitude of the second harmonic after correction and $A(2\omega)_{max}$ is the value measurement for the second harmonic amplitude when there is no intentional power loss in one arms and no phase difference between the arms.

1. Electroabsorption in the V_{set} Arm

For the case shown in Fig. 15, V_{set} applied to the 2 mm modulator and increased in successive steps from 10 to 24 V. In this voltage range, in addition to phase change, there was increased electroabsorption in the V_{set} arm of the interferometer so that a power imbalance was created between the arms. Phase measurement and correction proceeded as usual in 3 to 4 cycles with power loss of up to 90% in the V_{set} arms (observed form the decrease of the amplitude of the second harmonic and dc output).

2. Carrier Absorption in the V_{set} Arm

For the case shown in Fig. 16, the 2 mm modulator in the V_{set} arm of the interferometer was forward-biased, and the current I_{abs} successively increased from zero to 100 mA in steps of 10 mA. The power in the V_{set} arm of the interferometer was

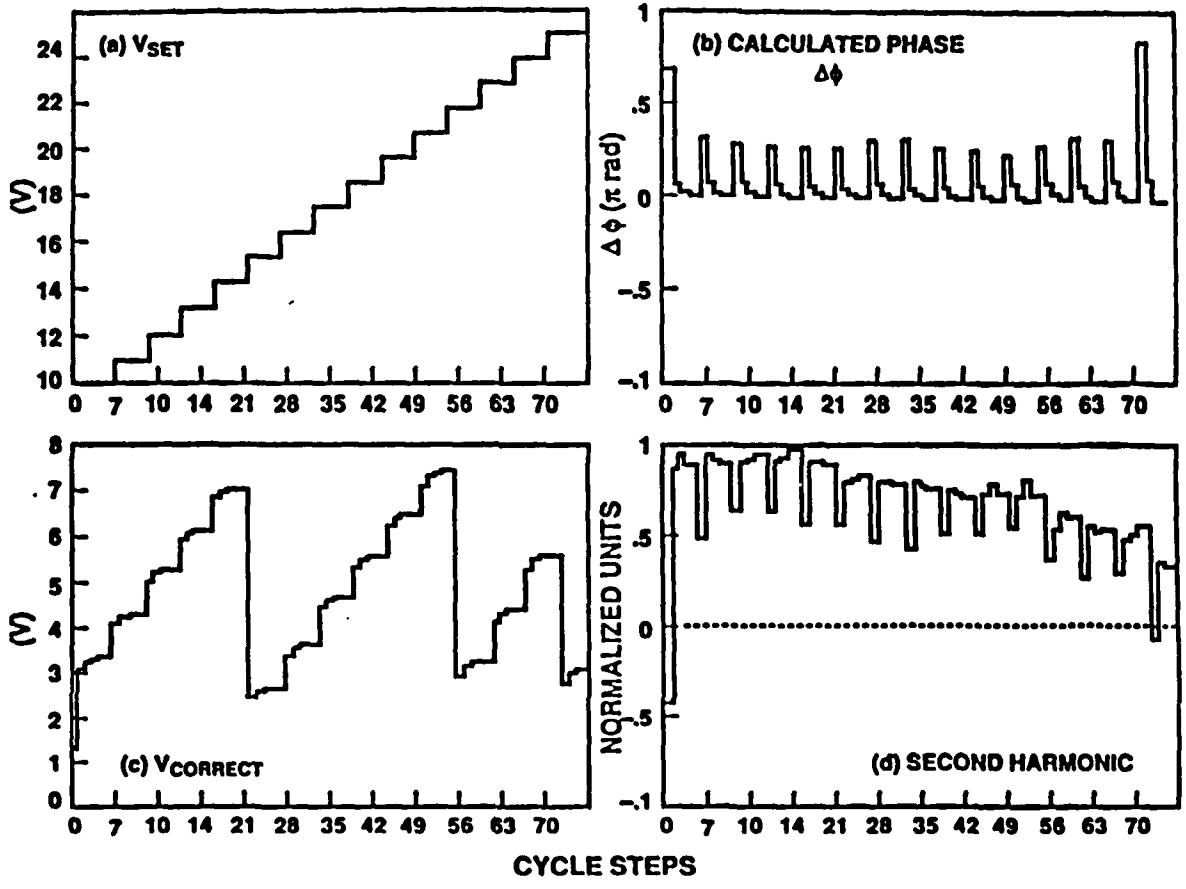

Fig. 15 Phase measurement and correction results with a power imbalance between the interferometer arms via electroabsorption in the V_{set} arm: (a) V_{set} applied to the 2 mm modulator and successively stepped from 10 to 24 V, (b) the calculated phase difference $\Delta\phi$ between the interferometer arms, (c) the applied correction voltage $V_{correct}$, and (d) the measured amplitude of the second harmonic (indicating a power loss of up to 90% in the V_{set} arm).

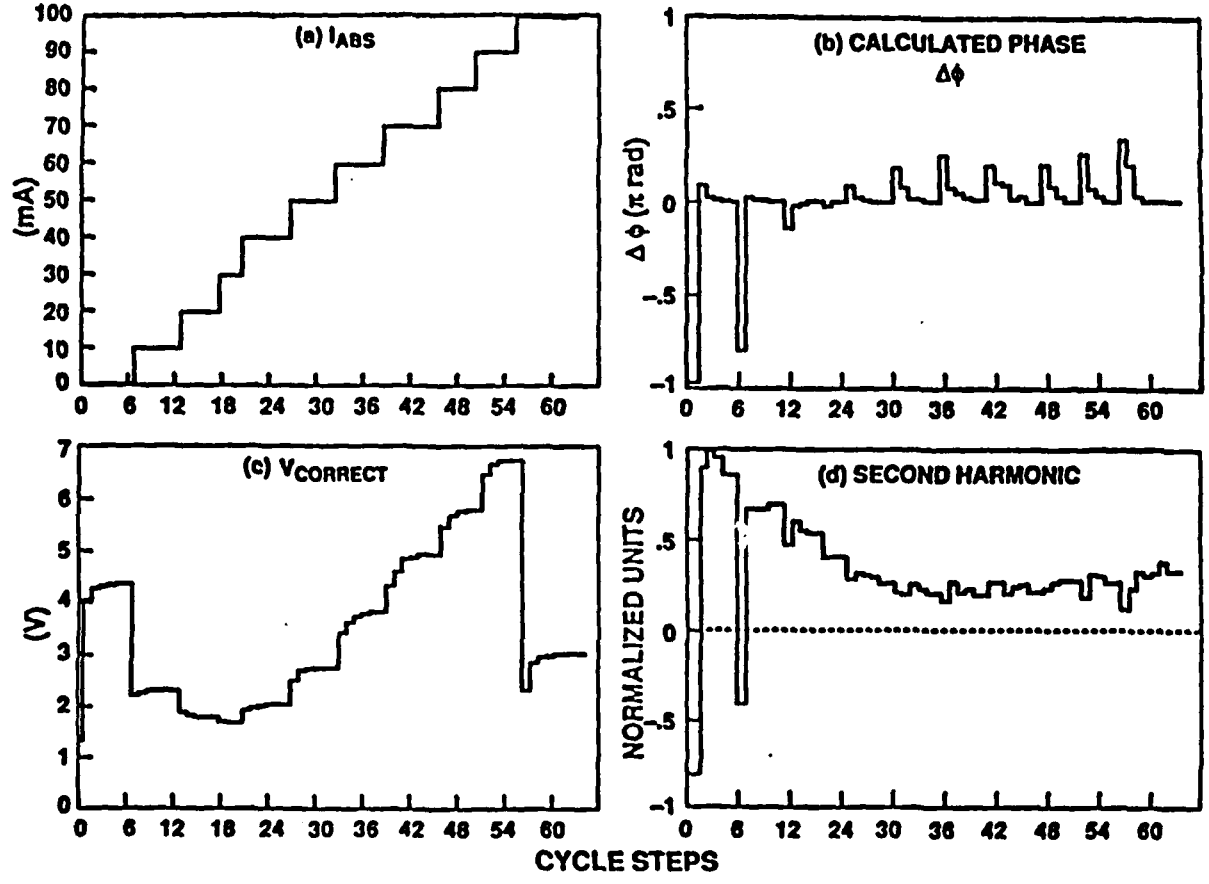

Fig. 16 Phase measurement and correction results with a power imbalance between the interferometer arms via carrier absorption in the V_{set} arm: (a) I_{abs} applied to the 2 mm modulator and successively increased from zero to 100 mA, (b) the calculated phase difference $\Delta\phi$ between the interferometer arms, (c) the applied correction voltage $V_{correct}$, and (d) the measured amplitude of the second harmonic (indicating a power loss of up to 93% in the V_{set} arm).

attenuated via carrier absorption, in addition to phase change. Measurement and correction of the applied difference was achieved in the usual 3-4 cycles with a power loss of up to 93% in the V_{set} arm.

In order to investigate phase difference measurement and correction performance of the Mach-Zehnder interferometer when there is a large power imbalance (with power ratio > 10:1) and a known applied phase difference between the interferometer arms, the following test cases were compared:

a. The 2 mm modulator was forward-biased with I_{abs} = 0 mA (no current flow, no power absorption). and V_{set} was applied to the 1 mm modulator and successively increased from zero to 10 V in steps of 2 V, (see Fig. 17 (a)). The resulting phase difference and correction voltage are shown in Fig. 17 (b) and (c).

b. The 2 mm modulator was forward-biased with I_{abs} = 80 mA (corresponding to a >90% power loss in the V_{set} arm), and V_{set} was again applied to the 1 mm modulator and successively increased from zero to 10 V in steps of 2 V, (see Fig. 17 (d)). The resulting phase difference and correction voltage are shown in Fig. 17(e) and (f).

In the first case, the power in the V_{set} arm of the interferometer arms was not intentionally attenuated and correction was achieved in the usual 3-4 cycles. In the second case, the power in the V_{set} arm of the interferometer was attenuated by more than 90% (corresponding to a power ration > 10:1 between the interferometer arms). The successive steps in applied phase difference were still corrected in 3-4 cycles.

This demonstrated conclusively that the phase difference measurement and correction performance of the interferometer was independent of the power or power ration in the interferometer arms for power ratios > 10:1.

3. Both Electroabsorption and Carrier Absorption in the V_{set} Arm

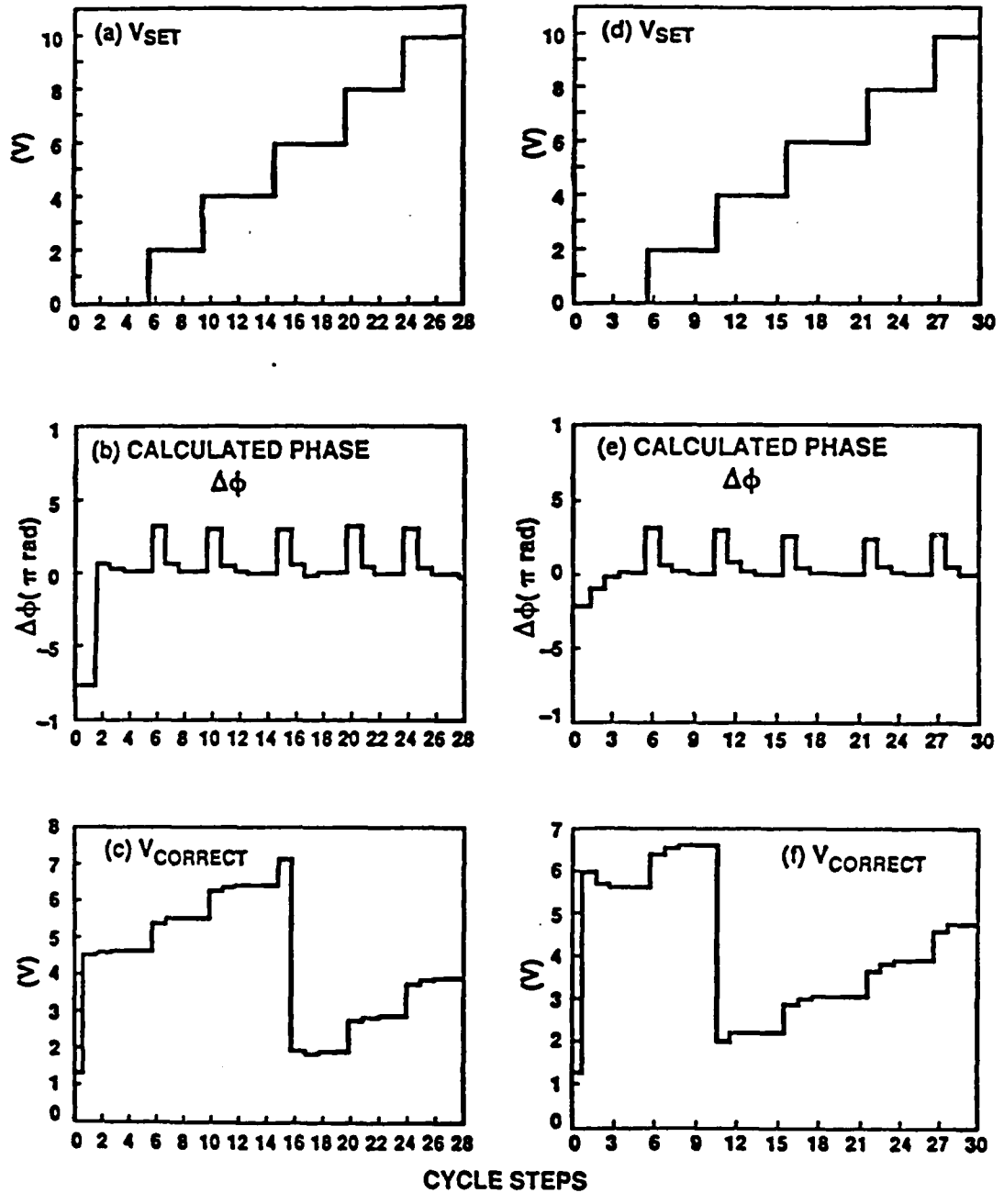

Fig. 17 Results for the cases when I_{abs} = 0 mA (no power loss) and I_{abs} = 80 mA (>90% power loss), respectively, were applied to the 2 mm modulator, and V_{set} applied to the 1 mm modulator was increased from zero to 10 V in steps of 2 V. The calculated phase difference Δφ between the interferometer arms, (b) and (e), and the applied correction voltage $V_{correct}$, (c) and (f), are shown for each case of I_{abs}.

As a final case, the 1 mm modulator in the V_{set} arm was first biased with no current (I_{abs} = 0 mA), the 2 mm modulator on the same arm was biased with 0 V and the phase difference between the interferometer arms was corrected. The 2 mm modulator was then reverse-biased with a voltage of 24 V, so that there was substantial electroabsorption in the arm, and the 1 mm modulator forward-biased with I_{abs} increasing from zero to 100 mA in steps of 10 mA. This resulted in power loss in the V_{set} arm due to both electroabsorption and carrier absorption. Phase correction for increasing I_{abs} was successfully achieved in the usual 3-4 cycles with a power loss of up to 98% in the V_{set} arm (shown in Fig. 18). This was the maximum power decrease that could have been achieved with the interferometer samples that were fabricated. Thus, in this case the phase difference measurement and correction performance of the interferometer was independent of the power or power ratio in the interferometer arms for power ratios > 50:1.

V. Fabrication of The Basic Module

The basic module for wavefront correction is shown in Fig. 1 of this report. The fabrication, operation and optimization of reduced-confinement GaAlAs tapered waveguide antennas for use in coupling to free-space radiation was described[3,4], and described in detail in our final report for the predecessor Air Force Contract #F49620-87-C-0043. The results presented in Sections III and IV of this report demonstrated that Mach-Zehnder interferometer system, proposed for the basic module, could both measure the phase difference at the output of the interferometer and reduce this phase difference to zero independent of power or power ratio in the interferometer arms. In this section the fabrication of the basic module (less the waveguide antennas) is described.

A. Waveguide Design and Modal Characteristics

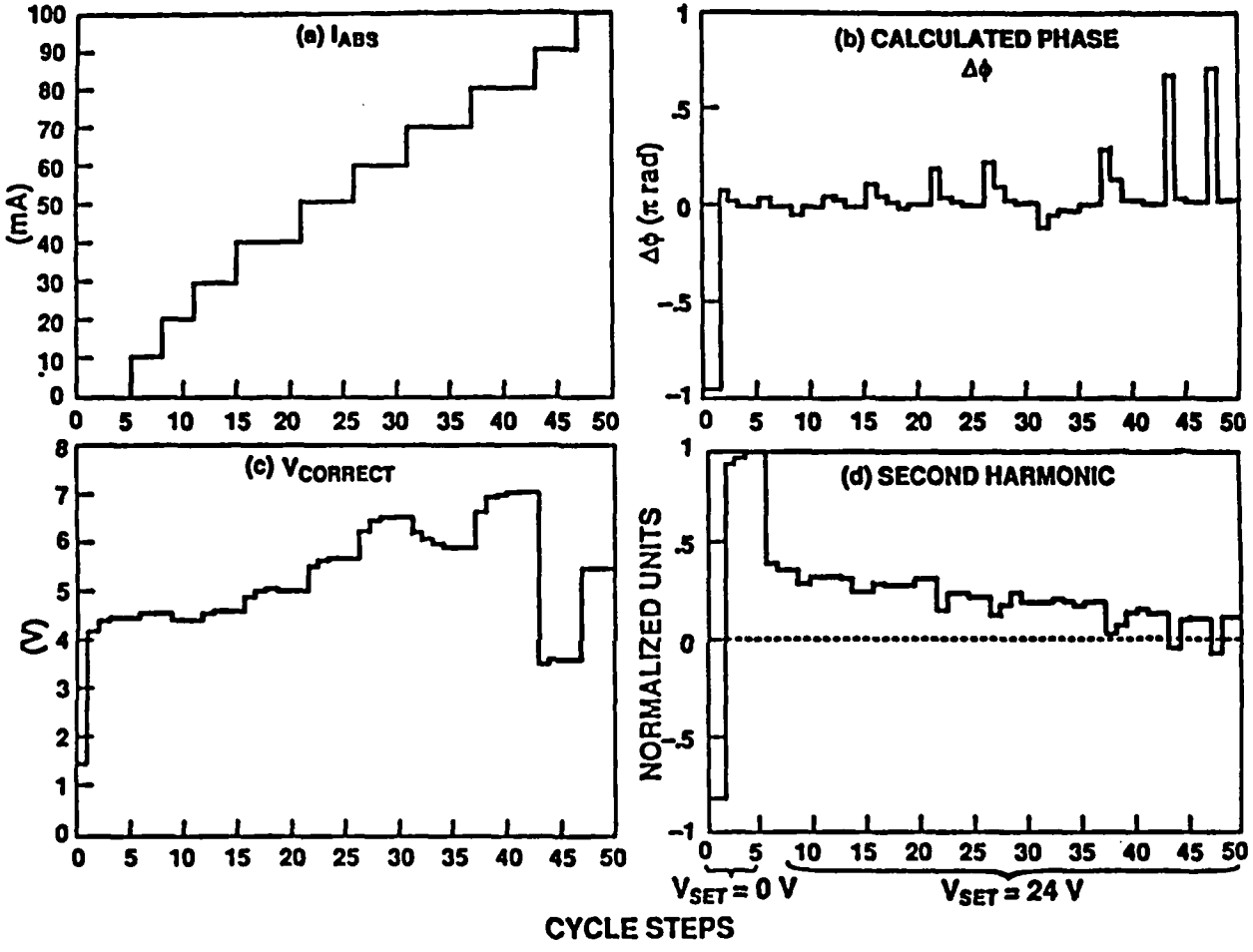

Fig. 18 Phase measurement and correction results with a power imbalance between the interferometer arms via both electroabsorption and free carrier absorption in the V_{set} arm: (a) I_{abs} applied to the 2 mm modulator and successively stepped from zero to 100 mA, (b) the calculated phase difference $\Delta\phi$ between the interferometer arms, (c) the applied correction voltage $V_{correct}$, and (d) the measured amplitude of the second harmonic (indicating a power loss of up to 98% in the V_{set} arm).

The fabrication parameters were adjusted so that they were compatible with fabricating all the components incorporated in the basic module. In this section the fabrication of the two new components developed for the basic module will be emphasized. The basic module is shown in the context of this section in Fig. 19. The phase modulators, which in Fig. 10 of Section III were incorporated in interferometer are now placed in the straight-through arms of the basic module as also shown in Fig. 1 which is at the beginning of this report. In building the basic module, the dielectric waveguide couplers had to be designed and fabricated. The dielectric waveguide coupler, evanescently couples a small fraction of the power in the straight-through waveguide into the adjacent arm of the interferometer between the waveguides. The fraction is denoted by the parameter δ in Eq. 1, also at the beginning of this report. A new component is the on chip integrated photodetector for the output of the interferometer. This on chip detector, shown as the box labeled D in Fig. 19, must be prelude to incorporating the circuitry for phase measurement and correction , which is now off chip, on chip. All the results of Section IV were obtained with an off-chip detector. Thoughout this project in the designs and fabrication described in Section III and this section , great care was taken and much effort was expended to ensure compatibility with the goal of monolithic integration in the future.

The cross-section of the dielectric-loaded strip heterostructure waveguide structure that was fabricated is shown in Fig. 20. This structure is similar to that of Fig. 4 with exceptions which will be noted below. One important dimension, not shown in Fig. 4, is upper cladding of thickness W_{2s}. This thickness is critical for the waveguide coupler. The waveguides are designed to propagate only the lowest guided mode. The composition, Al_xGa_yAs, of the individual dielectric slab layers shown in Fig. 20 is consistent with the fabrication of low loss waveguides for $\lambda = 0.83\mu m$. Moreover, this structure is fully compatible with the fabrication of other integrated optical

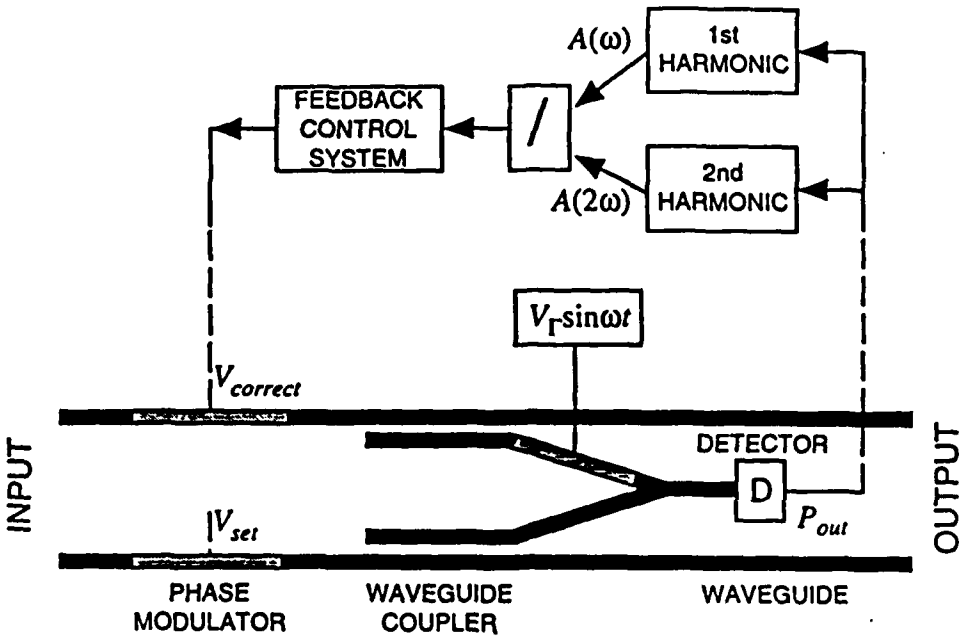

Fig. 19 Basic module for a phase measurement and correction system. $V_{correct}$ is used to control the relative phase, whereas V_{set} can be used to induce an intentional phase imbalance when testing the device.

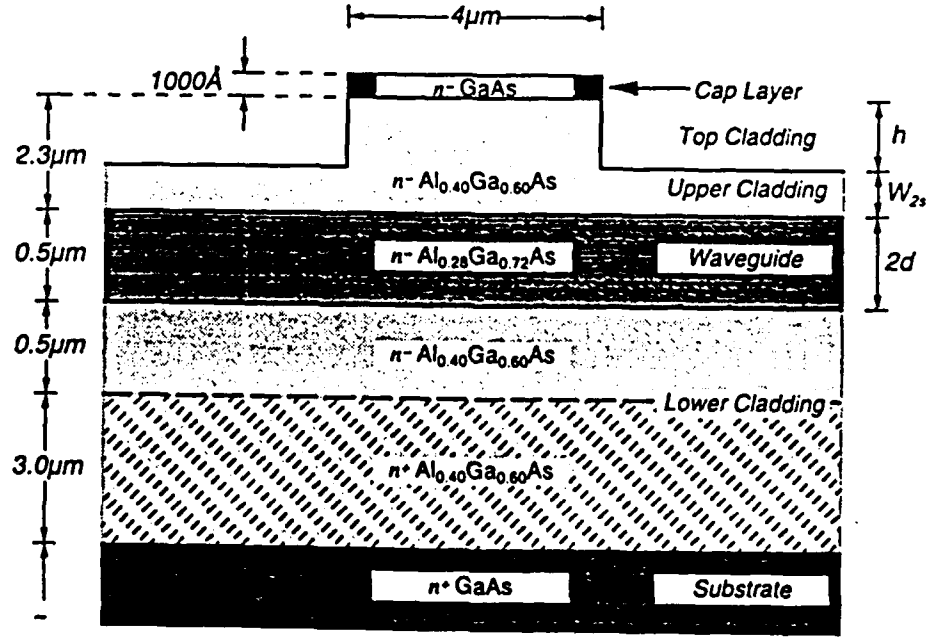

Fig. 20 Dielectric-loaded strip waveguide cross section.

components needed for this research. The n+ doped lower cladding region is not needed for the waveguide design, but it actually may be causing some guiding loss. However, this layer is required for the implementation of integrated phase modulators Once the composition and thicknesses of the individual dielectric layers was chosen, the device performance was determined by the specific wavelength used, waveguide rib width, and height. cladding thickness. A number of numerical simulations of loaded-strip structures using the layer composition shown in Fig. 20 was performed. For single mode operation, the rib width was chosen to be 4μm, and was set by the photolithographic mask used for waveguide patterning. This width yields good single mode performance and is large enough to ensure consistent fabrication results. Thus, the only fabrication dependent variable was the actual rib height, which was controlled through the etching process. The y-direction propagation constant, k, is shown as a function of wavelength λ, in Fig. 21. It is of interest to point out as can be seen in the figure that this particular loaded strip waveguide structure becomes more single mode as the wavelength decreases.

This counter intuitive behavior is a result of the change in the index of refraction of the individual AlGaAs layers with wavelength, and the change in the mode shapes of the four layer waveguide slabs it affects. With increasing wavelength, the effective index of the side region N_s changes faster than that of the rib region N_r, resulting in smaller mode confinement.

B. Waveguide Coupler Design

For fabricating waveguide couplers it is important to understand how the coupling changes as a function of design parameters. Since the coupler is in effect two waveguides in close proximity, the epitaxial layers used are identical to those used for the single-mode waveguides. Moreover, the width of the individual waveguides was set to be 4μm. Thus the fabrication dependent variables left were the guide separation S, the upper cladding in the side regions W_{2s} , and the actual interaction length between the two

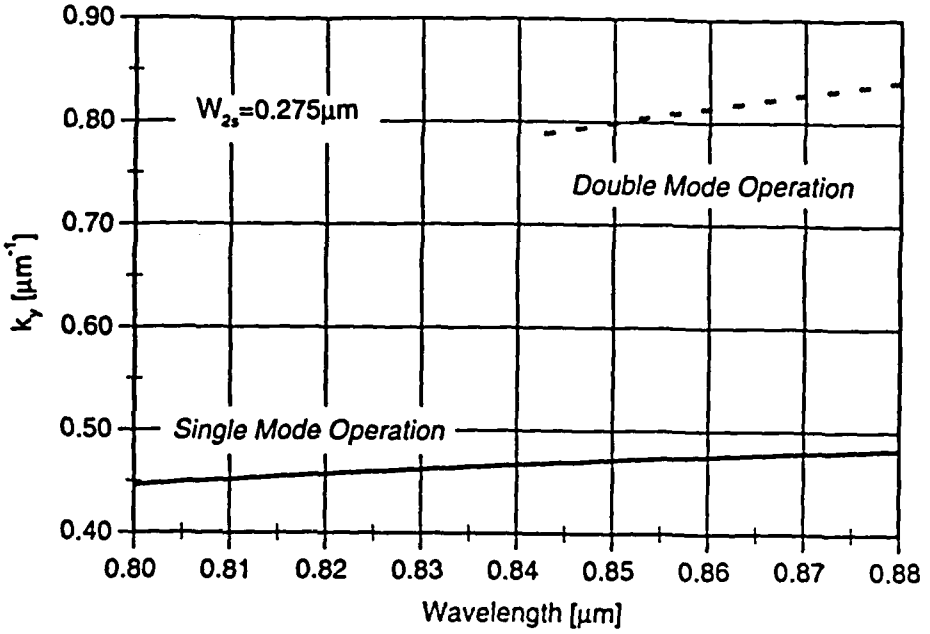

Fig. 21 Dependence of the y-direction propagation constant k_y on the wavelength.

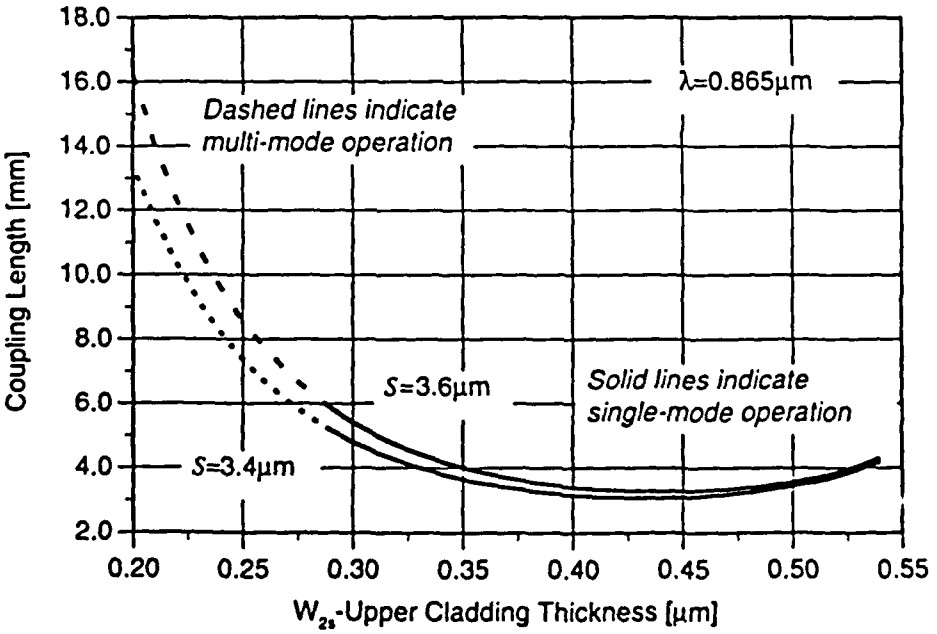

Fig. 22 The coupling length as a function of W_{2s} for two different guide separations.

waveguides. Two sets of devices were designed, each having different coupler parameters. One set of couplers was designed with guide separation S = 3.4μm, and the other with S = 3.6μm. Once the waveguide width and separation are fixed, the coupling between the waveguides becomes a function of W_{2s}. Figure 22 shows how the coupling length (needed to transfer all the power from one waveguide into the other) depends on W_{2s}. However, the couplers in this project were not used for full power transfer, but the interaction length was set to yield an approximate 0.10/ 0.90 power splitting ratio. The coupler with S=3.4 μm was made with an interaction length ℓ= 790μm, whereas the S=3.4 μm had an interaction length ℓ= 707μm. Figures 23 and 24 show how the predicted power transfer varies with W_{2s} for different wavelengths. The coupling coefficients k used in the numerical simulations were evaluated using the normal modes of the compound waveguide coupler structure. For the case of two identical, parallel waveguides, it was particularly easy to calculate the even and odd modes of the compound structure. One has to keep in mind that for the dielectric-loaded strip structures discussed both methods yield an approximate result since the effective index method was used to simplify the analysis. The above calculations did not take into account the effects of the transitions at the input or output of the actual waveguide coupler. The abrupt input transition, from one isolated to two coupled waveguides, will result in radiation losses. The weaker the coupling (the better the approximation), the lower the radiation losses. At the output, the two parallel coupler waveguides are gradually tapered away from each other and, therefore, extend the effective interaction length[9]. While a more rapid guide separation (large angle) decreases the interaction length it introduces larger radiation losses[10].

C. Integrated Photodetectors

When integrating waveguides and photodetectors onto the same device, the different material-composition requirements for the two have to be reconciled. The waveguides should have low loss at the wavelength used, whereas the photodetectors

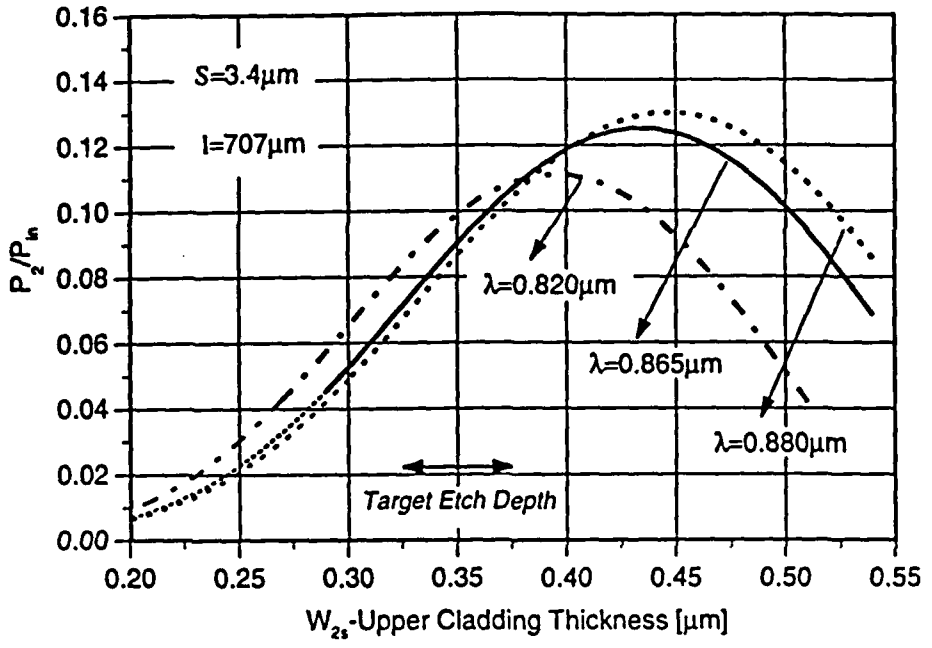

Fig. 23 Percentage of the input power transferred into guide 2 as a function of W_{2s} for S=3.4μm and l=707μm.

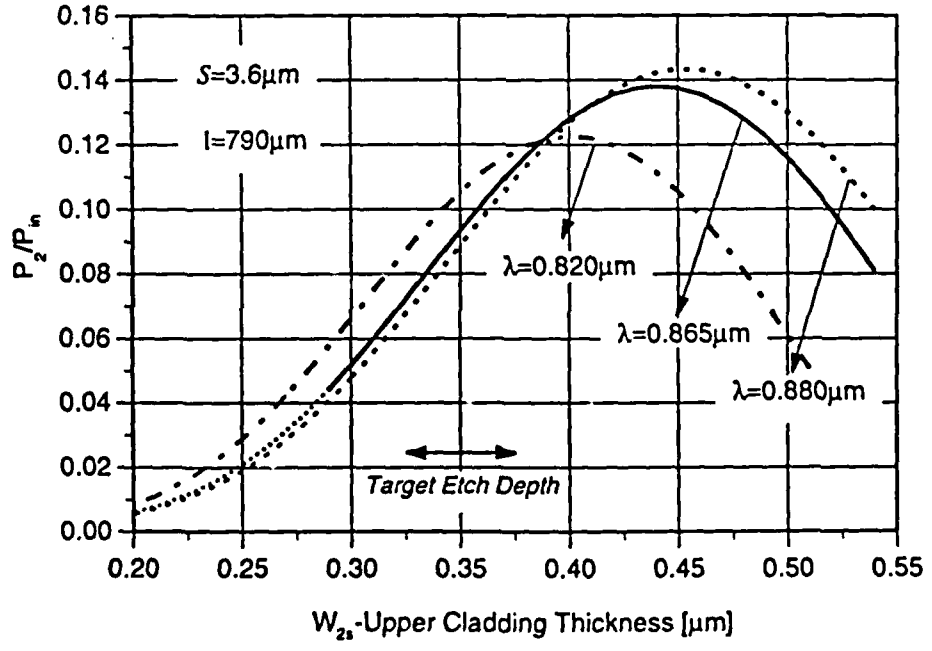

Fig. 24 Percentage of the input power transferred into guide 2 as a function of W_{2s} for S=3.6μm and l=790μm.

should have strong interband absorption for carrier generation. Thus, the choice of the integrated photodetector design was mainly dictated by its compatibility with the performance and fabrication requirements of the waveguides and integrated modulators. Three techniques to monolithically integrate detectors and waveguides are shown in Fig. 25. Butt-coupled detectors are placed as a termination of a waveguide making very efficient coupling possible. Moreover, a small interaction length, and a small area make them very suitable for high-speed applications. However, their major drawback is that their implementation requires an epitaxial regrowth of the absorbing detector layer. Another implementation of integrated photodetectors shown in Fig. 25 (b) is based on the evanescent-coupling approach . In this implementation, a vertically integrated structure is used, such that part of the power is coupled into a lossy region where detection occurs. This approach, though regrowth free, is incompatible with dielectric-loaded strip waveguides used in this project. The detector implementation chosen for this project is shown in Fig. 25 (c) and has been demonstrated by Bossi et al.[11]. The detector is an metal-semiconductor-metal (MSM) detector utilizing total-internal reflection (TIR) to couple light into the absorbing detection layer. This implementation does not require any epitaxial regrowth, and is fully compatible with the dielectric-loaded strip waveguides and modulators discussed previously.

1. Rectifying Metal-Semiconductor Junctions (Schottky Barrier Diodes)

Many of the useful properties of a p-n junction can be obtained by making an appropriate metal-semiconductor contact. The ease of fabrication, in addition to their high-speed performance potential, makes metal-semiconductor junctions of particular interest for integrated photodetector implementations. The forward current is due to the injection of majority carriers from the semiconductor into the metal.

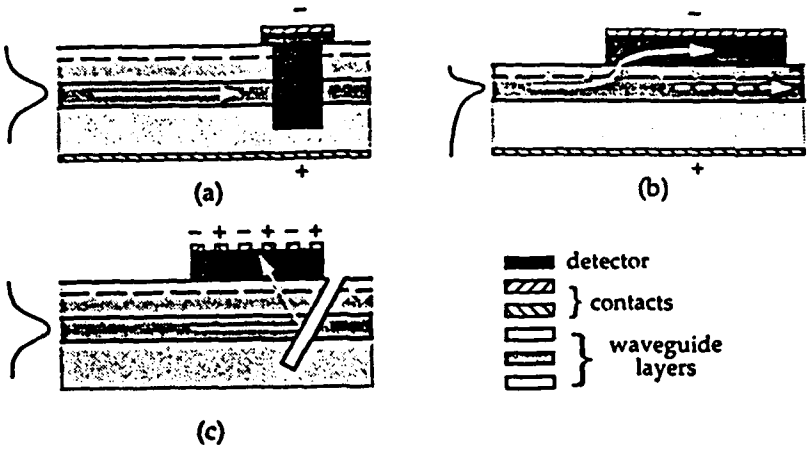

Fig. 25 Schematics of various integrated detector designs: (a) loaded strip waveguide and butt-coupled detector, (b) rib waveguide with evanescent-coupling detector, (c) loaded strip waveguide and MSM detector with TIR mirror coupling.

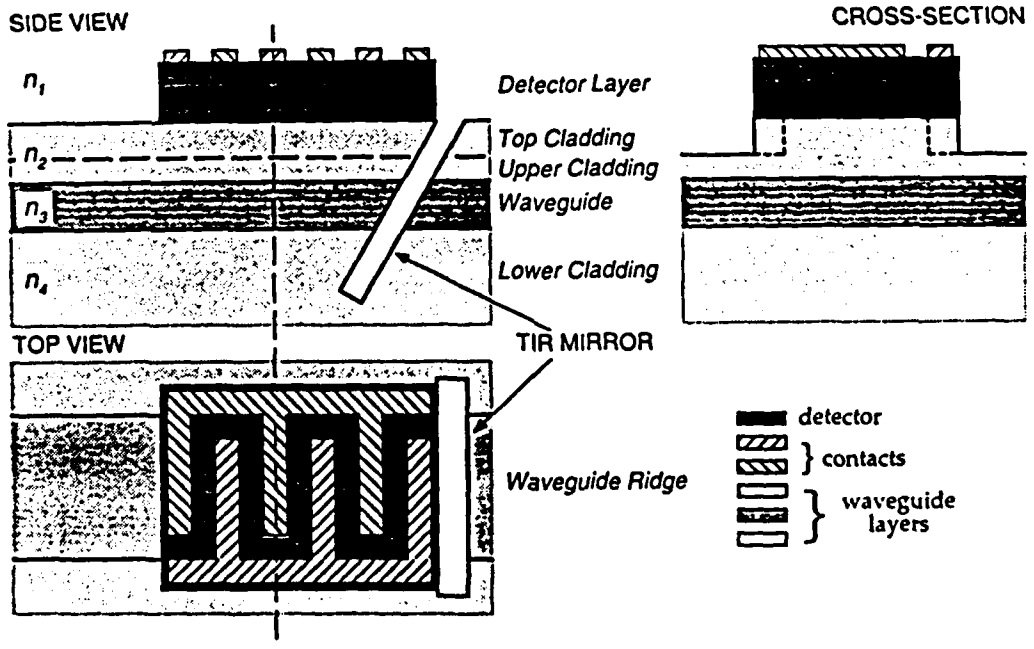

Fig. 26 Dielectric-loaded strip waveguide and MSM detector with TIR mirror coupling.

2. MSM Photodetector with TIR Coupling

The metal-semiconductor-metal (MSM) detector consists of two, back-to-back Schottky barriers. Two metal contacts are deposited onto a semiconductor (intrinsic) for which the bandgap is smaller than the frequency of the light which will be detected. To be used as a photodetector this device must be operated with an applied bias voltage. When a bias voltage is applied, one of the junctions becomes forward biased, whereas the other, reverse biased junction operates as a photodetector. The field in the depletion region of the reverse biased junction assures the collection of generated carriers. Whereas the forward biased junction allows the photocurrent (and dark current) to flow.

The dielectric waveguide and MSM detector with vertical integration made possible by the use of a TIR mirror is illustrated in Fig. 26. The absorbing detection layer is placed above the waveguide and does not compromise the low loss properties of the waveguide The TIR mirror is etched into the material such that the light is deflected upward, away from the waveguide, into the overlaying detection layer. Interdigitated electrodes are placed on top of the detector mesa. These are used for applying the necessary bias voltage, and measuring the generated photocurrent. The dielectric-loaded strip waveguide consists of dielectric slabs of different indices of refraction. For efficient coupling into the detection layer the TIR reflection condition has to be satisfied for all layers such that

$$\theta_{TIR} \geq a\sin(n_1/n_i) \ , \ n_i = 2....4 \qquad (7)$$

The lateral mode confinement is lost once the mode is under the detector, whereas the vertical component remains guided until the mode is reflected form the TIR mirror. Thus, the minimal detector area is determined by considering the mode size within the waveguide, and its increase due to unguided propagation.

3 Detector Design

The MSM detector was designed and fabricated such that it was fully compatible with other integrated optical components. The epitaxial waveguide modulator layers are kept unchanged but additional stop-etch and detector layers are grown on top. The optimized waveguide and modulator performance is not compromised by adding a 1.3 μm thick GaAs detector layer to the structure. The 500Å thick $Al_{0.60}Ga_{0.40}As$ stop-etch layer separating the waveguide and the detector material was needed to assure good fabrication results and has no operational significance. The detector and stop-etch layer were removed everywhere but in (17 μm x 69 μm) regions where the detectors were placed. The TIR mirror consisted of a groove etched at an angle greater than the critical angle θ_c. The value of θ_c was determined by the index difference between the AlGaAs layers and the TIR mirror material. For the simplest case this would be air, however, it was decided to coat the TIR mirrors with a SiO_2 layer for protection. Since the index difference between AlGaAs and SiO_2 results in a larger θ_c, the latter was chosen to determine the TIR mirror angle θ of 30° with respect to the sample normal. The groove forming the TIR mirror was about 6 μm deep and (10 μm x 13 μm) in area.

The interdigitated Ti/Au detector contacts were 2 μm wide fingers with 2 μm spacing between them. These fingers were connected to the contact pads used for applying a desired bias voltage and for measuring the generated photocurrent.

VI. Device Characterization Measurements

A. Waveguide Phase Difference Measurement

Figure 27 shows the experimental setup used for measuring the phase difference between two waveguides. To characterize the integrated modulators and verify the interferometer operation the output was recorded as a function of the reverse-bias voltage applied to one of the 2.0 mm modulators. The other 2.0 mm modulator was driven by a sinusoidal dither signal with an dc. voltage offset V_{offset} to assure that the

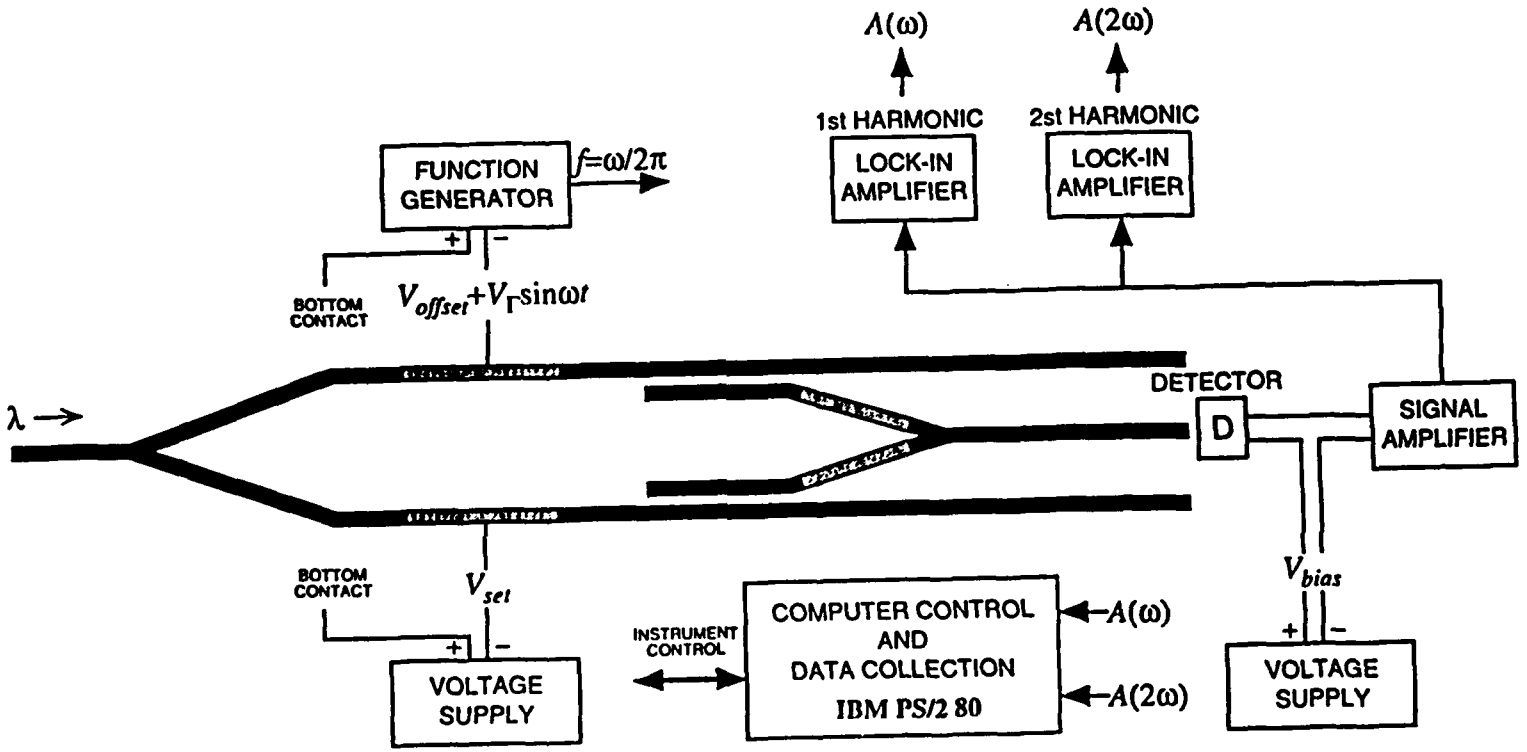

Fig. 27 Characterization of the modulator and interferometer performance. The phase difference between the waveguides can be measured using the integrated interferometer. The phase can be set by applying a voltage to the integrated phase modulator.

modulator remains reverse biased at all times. The data obtained using the phase dither approach confirmed the predicted linear voltage/phase relationship for the fabricated modulators. To demonstrate the interferometer and modulator operation an external photodetector was used for recording the interferometer output signal. The modulatorr everse-bias voltage V_{set} was stepped from 0 to 25V in steps of 0.25V. Measurements of the interferometer output were conducted for several dither amplitudes and offset voltages V_{offset}, always assuring that the modulators were reverse biased at all times. A typical set of data, obtained using a dither amplitude V_Γ=2.0V is shown in Fig. 28 . The voltage needed for obtaining a π phase-shift was V_π=5.0V. Equation 8 which is the same as Eq. 5 in Section III was used to successfully recover the phase difference between the two adjacent straight-through waveguides.

$$\Delta\phi = \arctan\left[\frac{A(\omega)}{A(2\omega)}\frac{J_2(\Gamma)}{J_1(\Gamma)}\right] = \arctan\left[\frac{A(\omega)}{A(2\omega)}\frac{\frac{\Gamma^2}{8}-\frac{\Gamma^4}{96}+\cdots}{\frac{\Gamma}{2}-\frac{\Gamma^3}{16}+\cdots}\right] \qquad (8)$$

The Bessel functions in Equation (8) were calculated using the first two terms and the simple linear relationship for the amplitude of the phase dither $\Gamma = \pi V_\Gamma / V_\pi$. The range of phase angles was chosen such that it always falls in the range between $-\pi$ and $+\pi$. This particular phase range is arbitrary since the phase could have been represented by any 2π interval. The breakdown voltages for the modulators were in excess of 40V. Using the setup in Figure 27 the phase between two adjacent waveguides was successfully recovered. An external Germanium detector was used for detecting the interferometer output signal. A 200 μm pinhole was placed in front of the detector to block-out stray light from hitting the detector. The first and second dither harmonic were separated with lock-in amplifiers and the amplitudes were sent to the computer where the phase was calculated using Equation 8. The nonlinearity in the recovered phase for V_{offset} = 2.5V

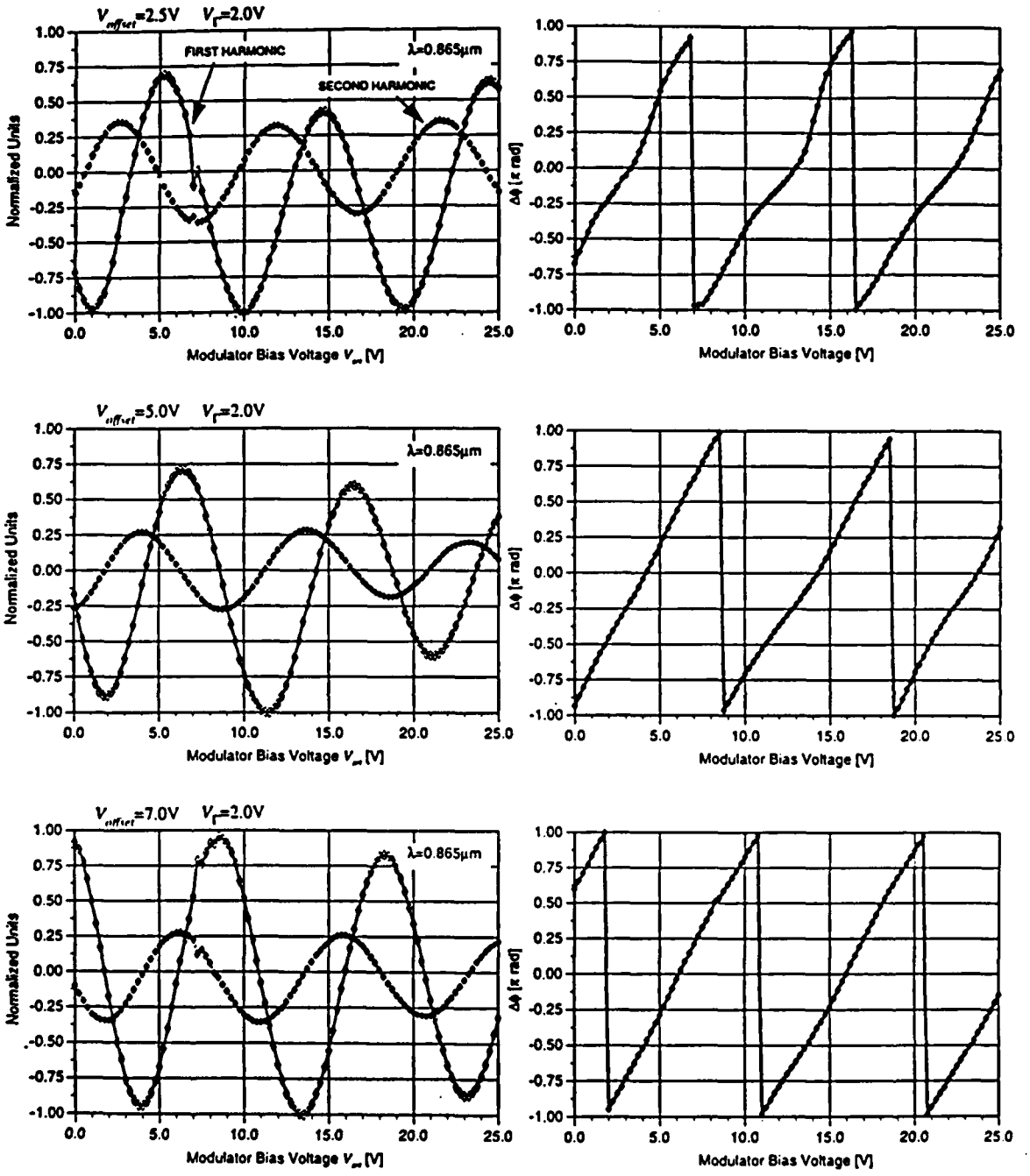

Fig. 28 Typical interferometer outputs obtained using the setup shown in Fig. 27. On the left are measured amplitudes for the first and second harmonic of the detector signal. The corresponding calculated phase differences between the two waveguides are shown on the right.

is not due to a fundamental device limitation. To reduce the need for additional processing steps, the top modulator contact was not an ohmic contact. Since this contact was deposited in the same fabrication step as the detector electrodes, Schottky barrier modulator contacts were obtained. To punch-though the Schottky barrier and the modulator layers, bias voltages of $V_{offset} \geq 5.0$ V were used on dither electrode in order to obtain the desired phase information. To measure the coupling coefficient the power in the straight-through waveguides and the signal at the interferometer output were measured. The power splitting for the couplers was calculated to be ≈ 0.02. The upper cladding thickness in this portion of the device was measured to be 0.23μm, thus, the experimentally obtained coupling coefficient is in close agreement with the theoretically calculated values shown in Figure 24. The waveguide outputs were imaged on a CCD camera to determine the mode profile. The fabricated waveguides were 4.0μm wide and, as predicted by the theoretical modeling, the waveguide outputs were single-mode.

B. Waveguide Phase Difference Measurement with an Integrated Photodetector

The sample tested in this section was fabricated to demonstrate the phase measurement using an integrated photodetector for recording the interference signal. This device was successfully used to demonstrate the phase measurement with all optic and opto-electronic components needed integrated on the same device. The interferometer output shown in Figure 29 recorded as the function of the reverse-bias voltage on the 2.0 mm phase modulator. The other 2.0 mm phase modulator was used for dithering the phase difference. The data obtained were in close agreement with the those obtained using the external detector.

The modulator reverse-bias voltage V_{set} was stepped from 0 to 25V in steps of 0.25V. Measurements of the interferometer output are shown in Fig. 30 for a dither amplitude of 1.0V and offset voltages V_{offset}=5.0 and 7.0V. The voltage needed for obtaining a π phase-shift was V_{π}=4.6V. The integrated MSM detector was biased at

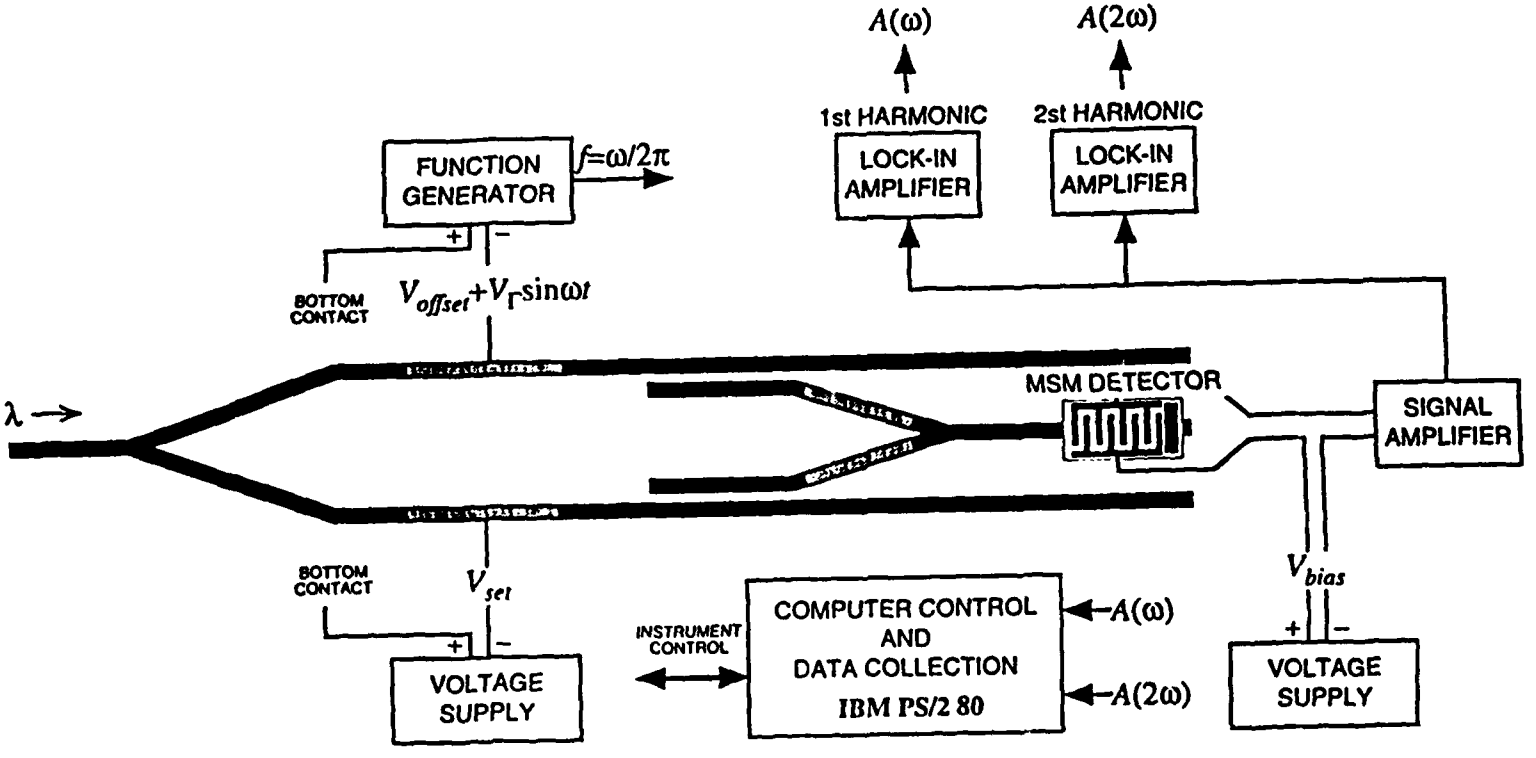

Fig. 29 Characterization of the waveguide phase difference measurement and correction device. Waveguides, modulator, and integrated detector were fabricated on the same sample.

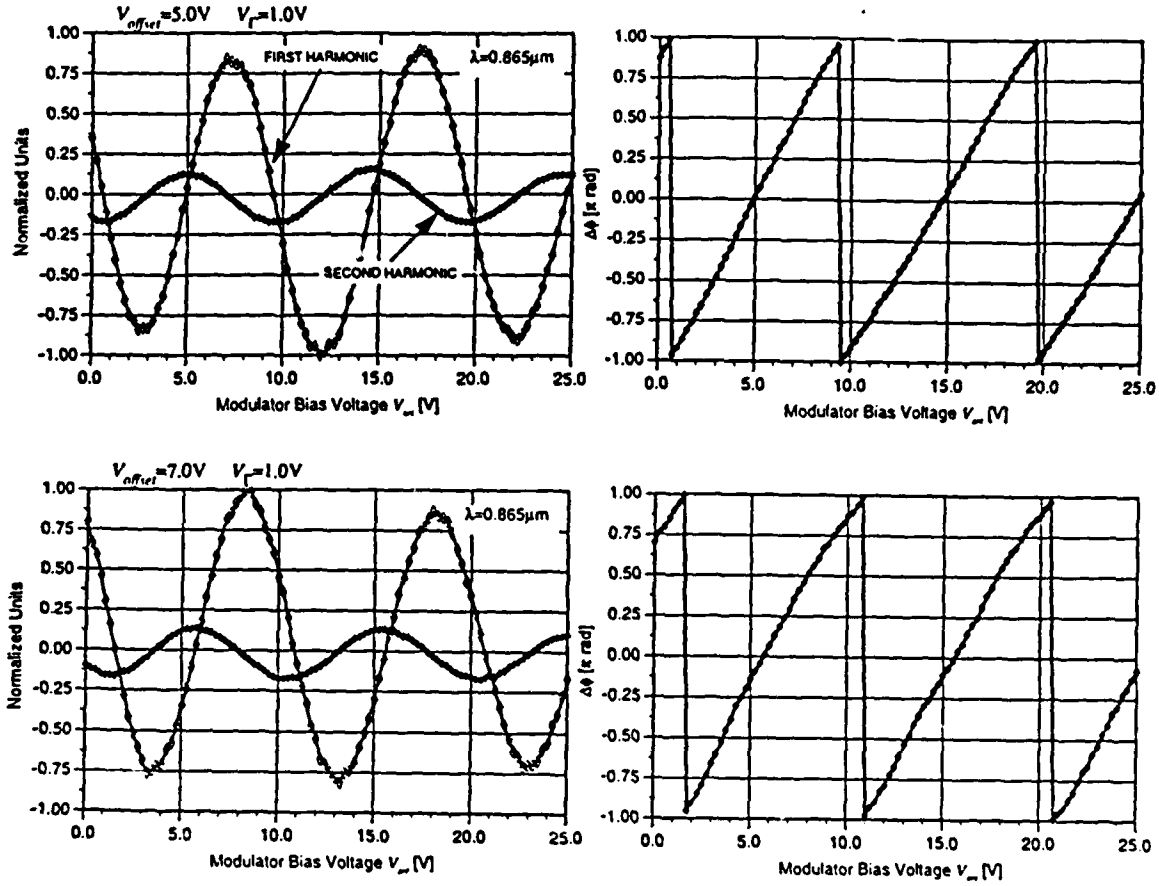

Fig. 30 Typical interferometer outputs obtained using the setup shown in Figure 29. On the left are measured amplitudes for the first and second harmonic of the detector signal. The corresponding calculated phase differences between the two waveguides are shown on the right.

9.0V, and the detector signal was fed into the lock-in amplifiers. The first and second dither harmonics were sent to the data acquisition computer where the phase difference was calculated. The phase was calculated using Eq. 8, and the device yielded the predicted linear voltage/phase relationship was obtained. All phase data presented were collected by applying the phase dither to one of the 2.0 mm modulators. Thus the dither applied to the interferometer had an amplitude 0.02 V The 2.0 mm modulators were chosen since changes in the applied bias to the 1.0 mm modulators (on the Y-junctions) resulted in changes in the coupling between the modulated Y-junction waveguide and the pass-through waveguide. The bias dependent coupling changed the signature of the first and second harmonic making it difficult to reliably recover the waveguide phase difference information. This coupling does not represent a fundamental device limitation but is a result of the close proximity of all optical components. In the next generation device, etched grooves similar to the ones routinely etched between the straight-through waveguides will be placed as shown in Fig. 31 between the straight-through and Y-junction waveguides, as well as between the Y-junction arms. The etched grooves will eliminate the undesired coupling and make it possible to reliably use the Y-junction modulators for phase dithering.

The data shown in Figure 30 show the successful implementation of a module that can measure and control the phase difference between two waveguides by using a small portion of the signal in the straight-through waveguides for phase measurements. All required waveguides (straight guides, bends, junctions, and couplers), modulators, and the photodetector were fabricated on the same GaAs/AlGaAs sample. The integrated photodetector was made small enough (17 μm x 69 μm) to fit between the two straight-through waveguides and was successfully used for phase measurements.

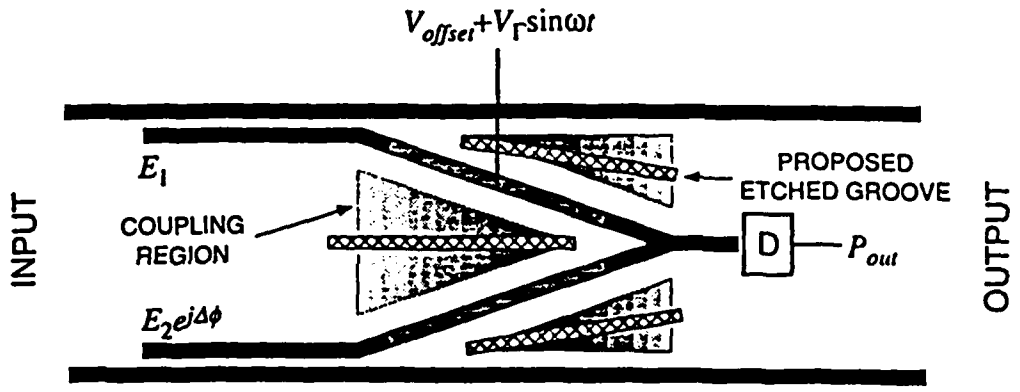

Fig. 31 Proposed device modification such that the Y-junction phase modulators can be used for applying the phase dither. Grooves are etched to eliminate coupling between adjacent waveguides.

References

[1]R.H. Rediker, T.A. Lind, and B.E. Burke, "Optical Wavefront Measurement and/or Modification Using Integrated Optics," J. Lightwave Tech., Vol. 6, pp. 916-932, 1988.

[2]F.J. Leonberger and J.P. Donnelly, "Semiconductor Integrated Optic Devices," in Guided-Wave Optoelectronics, ed. T. Tamir (Berlin: Springer-Verlag, 1988).

[3]D.E. Bossi, W.D. Goodhue, L.M. Johnson, and R.H. Rediker, "Reduced-Confinement GaAlAs Integrated Optical Waveguides," Appl. Phys. Lett., Vol. 56, pp. 420-422, 1990.

[4]D.E. Bossi, W.D. Goodhue, L.M. Johnson, and R.H. Rediker, "Reduced-Confinement GaAlAs Tapered Waveguide Antennas for Enhanced Far-Field Beam Directionality," IEEE J. Quantum Electron., Vol. QE-27, no. 3, pp. 687-695, 1991.

[5]R.H. Rediker, F.J. Leonberger, and D.P. Greenwood, "Method and Apparatus for Processing Optical Wave Signals," U.S. Patent 4,798,437, issued January 17, 1989.

[5]T.G. Giallorenzi, J.A. Bucaro, A. Dandridge, G.H. Sigel, Jr., J.H. Cole, S.C. Rashleigh, and R.G. Priest, "Optical Fiber Sensor Technology," IEEE J. Quantum Electron., Vol. QE-18, no. 4, pp. 626-665, April 1982.

[7]G.W. Johnson, D.C. Leiner, and D.T. Moore, "Phase-locked Interferometry," Opt. Eng., Vol. 18, no. 1, pp. 45-52, 1979.

[8]M.W. Austin and P.C. Kemeny, "Measurement of Semiconductor Optical Waveguide Loss Using a Pabry-Perot Interference Technique," Integrated Optics, eds. H. P. Nolting and R. Ulrich, Berlin: Springer-Verlag, pp. 140-143, 1985.

[9]Damask, J.N., "A New Photonic Device: The Integrated Resonant Channel-Dropping Filter," MIT S.M. Thesis, 1993.

[10]Lau, S., Donnely, J.P., Wang, C.A., Goodman, R.B., and Rediker, R.H., "Optical Phase Difference Measurement and Correction Using AlGaAs Integrated Guided-Wave Components," IEEE Photon. Technol. Lett., vol. 3, no. 10, 902-904, 1991.

[11]Bossi, D.E., Ade, R.W., Basilica, R.P., and Berak, J.M., "Regrowth-Free Waveguide-Integrated Photodetector with Efficient Total-Internal-Reflection Coupling," IEEE Photon. Technol. Lett., vol. 5, no. 2, 166-169, 1991.